

# Beyond Hertzsprung-Russell

A New Three Dimensional Diagram Including Temperature,  
Mass, and Radius

Oliver Zbinden

Master Thesis  
Astrophysics and Cosmology

Physik Institut  
University of Zurich  
February 2021

Supervisor:

Prof. Dr. Prasenjit Saha

# Abstract

Based on data from recent observation, we introduce a new diagram in stellar astrophysics that can be seen as three-dimensional alternative to the Hertzsprung-Russell diagram (HRD). Technical improvements allow nowadays to measure physical quantities of a high amount of stars very accurately. Therefore, the luminosity is probably, besides surface temperature, not anymore the fundamental quantity just because it is easy to measure. Our new diagram has axes of surface temperature, mass, and radius of stars, where the mass is calculated from surface gravity and radius. Especially the inclusion of the stellar mass is interesting because it is the quantity that has the strongest influence on how a star evolves. As an addition, colour is used to show the metallicity as a fourth dimension because it is the second quantity that influences stellar evolution significantly. The diagram, in two-dimensional projections, is compared to the HRD, and advantages and peculiarities are discussed.

Furthermore, we tested a simple method to estimate stellar ages, but with limited success. However, showing theoretical isochrones in our new diagram together with the obtained estimates, it seems that the stars are kind of layered by age in our diagram. This is not visible in the HRD by direct comparison. Further tests and more accurate observation would be required to make a final statement about this.

# Abstract German

Basierend auf neuen Messungen präsentieren wir ein neues Diagramm in der Astrophysik, welches als dreidimensionale Alternative zum Hertzsprung-Russell Diagramm (HRD) betrachtet werden kann. Fortschritte in der Technik erlauben heutzutage, dass physikalische Größen in einer Qualität und Quantität gemessen werden können, die bis anhin unerreicht waren. Daher ist, neben der Oberflächentemperatur, die Helligkeit der Sterne nicht mehr die fundamentale Größe, nur weil sie einfach zu messen ist. Unser neues Diagramm beinhaltet die Oberflächentemperatur, die Masse und den Radius der Sterne, wobei die Masse aus dem Radius und der Oberflächengravitation berechnet wurde. Insbesondere die graphische Darstellung der Masse ist interessant, da sie den größten Einfluss darauf hat, wie sich ein Stern entwickelt. Zusätzlich ist die Metallizität, welche auch einen wichtigen Einfluss auf die Evolution eines Sternes hat, durch Farben dargestellt. Das Diagramm wird dann, durch zweidimensionale Projektionen, mit dem HRD verglichen und die Vorteile und Besonderheiten werden aufgezeigt.

Zudem testeten wir eine einfache Variante, um das Alter von Sternen abzuschätzen, was jedoch nicht sehr gut gelang. Jedenfalls zeigen theoretische Isochronen zusammen mit den geschätzten Werten für das Alter, dass die Sterne in unserem Diagramm nach Alter scheinbar geschichtet sind, was im direkten Vergleich im HRD nicht ersichtlich ist. Es sind jedoch weitere Tests und genauere Daten notwendig, um eine definitive Aussage zu treffen.

# Contents

<b>1 The Evolution of Stars</b>	<b>1</b>
1.1 Structure Equations . . . . .	1
1.2 Energy Transport . . . . .	2
1.2.1 Radiative Energy Transport . . . . .	3
1.2.2 Convective Energy Transport . . . . .	3
1.3 Stellar Evolution . . . . .	4
1.3.1 Pre Main-Sequence . . . . .	4
1.3.2 Main-Sequence . . . . .	5
1.3.3 Late-time Evolution . . . . .	6
<b>2 Methods</b>	<b>8</b>
2.1 Data acquisition . . . . .	8
2.2 Friends of Friends . . . . .	10
2.3 Evolutionary Tracks . . . . .	10
2.4 Isochrones . . . . .	11
<b>3 Diagrams in Stellar Astrophysics</b>	<b>12</b>
3.1 The Hertzsprung-Russell Diagram . . . . .	12
3.2 A New Three Dimensional Diagram . . . . .	13
3.3 Comparison between the Diagrams . . . . .	15
<b>4 Age Determination</b>	<b>20</b>
4.1 Procedure . . . . .	20
4.2 Age estimation . . . . .	20
4.3 Validity test . . . . .	22
<b>5 Conclusion</b>	<b>24</b>
<b>List of Figures</b>	<b>25</b>
<b>List of Tables</b>	<b>26</b>
<b>A Jeans Mass</b>	<b>27</b>
<b>B Virial Theorem</b>	<b>28</b>
<b>C Luminosity increase</b>	<b>29</b>
<b>D M-T diagram</b>	<b>29</b>
<b>E Simple age validity test</b>	<b>30</b>
<b>F Observations and Isochrones</b>	<b>34</b>
<b>References</b>	<b>38</b>

# 1 The Evolution of Stars

This section should only give an overview of stellar evolution that the reader is familiar with the topic, to understand the following sections. Many descriptions are simplified and some topics are skipped, but can be found in great detail in the indicated literature.

## 1.1 Structure Equations

The evolution of non-rotating stars is described by the stellar structure equations<sup>1</sup>. Under the assumptions of spherical symmetry they can be written as (e.g. Kippenhahn et al. 2012):

$$\frac{\partial r}{\partial m} = \frac{1}{4\pi r^2 \rho}, \quad (1)$$

$$\frac{1}{4\pi r^2} \frac{\partial r}{\partial t} = -\frac{\partial P}{\partial m} - \frac{Gm}{4\pi r^4}, \quad (2)$$

$$\frac{\partial L}{\partial m} = (\varepsilon_{nuc} - \varepsilon_\nu) - T \frac{\partial s}{\partial t}, \quad (3)$$

$$\frac{\partial T}{\partial m} = -\frac{GmT}{4\pi r^4 P} \nabla, \quad (4)$$

as well as the temporal evolution of the nuclear abundances

$$\frac{\partial X_i}{\partial t} = \frac{m_i}{\rho} \left( \sum_j r_{ji} - \sum_k r_{jk} \right), \quad i = 1, \dots, I, \quad (5)$$

which is not considered as a structure equation but still is very important. The variables are radius  $r$ , pressure  $P$ , temperature  $T$ , luminosity  $L$ , the mass fractions  $X_1, \dots, X_I$  of all occurring elements, time  $t$ , and  $G$  is the gravitational constant.

In case of hydrostatic equilibrium, the term on the left hand side of (2) vanishes. The terms in brackets on the right hand side of (3) describe the energy per unit mass per second  $\varepsilon_{nuc}$  released by nuclear processes, and the energy loss per unit mass per second  $\varepsilon_\nu$  due to the produced neutrinos that leave the star without interaction. The nuclear reaction rate, the number of reactions per unit volume and time that transforms nuclei from type  $l$  to type  $m$ , is described by  $r_{lm}$  in (5). Furthermore,  $r_{ml} = -r_{lm}$ .

In (4),  $\nabla \equiv d \ln(T) / d \ln(P)$ . The effective temperature gradient is

$$\nabla = \frac{d \ln(T)}{d \ln(P)} = \min(\nabla_{ad}, \nabla_{rad}), \quad (6)$$

with

$$\begin{aligned} \nabla_{rad} &= \frac{3}{16\pi acG} \frac{\kappa LP}{m T^4}, \\ \nabla_{ad} &= \left. \frac{\partial \ln T}{\partial \ln P} \right|_s. \end{aligned} \quad (7)$$

If the star is rotating, assuming the rotation is uniformly and constant in time, (2) becomes

$$\frac{\partial r}{\partial m} = \frac{1}{4\pi r^2 \rho} + \frac{2}{3} \omega^2 r \rho, \quad (8)$$

---

<sup>1</sup>(1): mass conservation, (2): hydrostatic equilibrium, (3): energy conservation, (4) energy transport equation, (5) variation of composition.

where  $\omega$  is the rotation rate. Therefore, we are left with  $4 + I$  differential equations with  $4 + I$  variables  $r$ ,  $P$ ,  $T$ ,  $L$ , and  $X_1, \dots, X_I$  of all occurring elements. The independent variables are  $m$  and  $t$ , or  $r$  and  $t$ .  $M$ ,  $R$ , and  $T_{\text{eff}}$  are the respective values of  $m$ ,  $r$ , and  $T$  at the stellar surface.  $\kappa$  is the opacity,  $c$  the speed of light, and  $\rho$  the density. To solve the four structure equations we have to specify four boundary conditions, two at the centre, and two at the surface of the star (Kippenhahn et al. 2012, MacDonald 2015). The central conditions for  $m = 0$  are obviously

$$\begin{aligned} r &= 0, \\ L &= 0. \end{aligned} \tag{9}$$

It would also be possible to take the central pressure  $P_c$  as an initial condition instead of  $L$ . But since this is an unknown, one would have to apply a shooting method to find an approximation of  $P_c$  that leads to the desired surface conditions. The first guessed surface boundary conditions are  $P \rightarrow 0$  and  $T \rightarrow 0$  as  $m \rightarrow M$  (or  $r \rightarrow R$ ), where 0 does not really mean zero, but considered to be negligible compared to the central conditions  $P_c$  and  $T_c$ . A more precise way is to determine the stellar radius  $r = R$  where the optical depth  $\tau$  has a value of  $\tau = 2/3$  with

$$\tau = \int_R^\infty \kappa \rho dr = \bar{\kappa} \int_R^\infty \rho dr. \tag{10}$$

Here,  $\bar{\kappa}$  is the mean opacity averaged over the stellar atmosphere. Now one can determine the pressure at the calculated radius,

$$P_{r=R} = \int_R^\infty g \rho dr = g_0 \int_R^\infty \rho dr = \frac{2}{3} \frac{GM}{\bar{\kappa} R^2}, \tag{11}$$

with surface gravity  $g_0 = \frac{GM}{R^2}$ . One can make the assumption that the photosphere of a star radiates in a black body spectrum<sup>2</sup>, peaking at the so-called effective temperature. Using Stefan-Boltzmann's law

$$L = 4\pi R^2 \sigma T_{\text{eff}}^4, \tag{12}$$

where  $\sigma$  is the Stefan-Boltzmann constant, we have a relation between  $T_{\text{eff}}$ ,  $R$ , and  $L$ , where the surface temperature is defined as  $T_{\text{eff}} = T_{r=R}$ . To obtain solutions of the structure equations one has to choose initial values as well, such as the initial stellar mass  $M_{\text{ini}}$  and the initial chemical composition with the conditions  $X + Y + Z = 1$  where  $Z \ll X, Y$ . Here,  $X$ ,  $Y$ , and  $Z$  are the hydrogen, helium, and metal mass fractions, respectively. These equations have to be solved numerically, as described in section 2.

## 1.2 Energy Transport

The light we see from stars is energy in form of visible electromagnetic waves that are emitted from its surface, the photosphere. This visible light is only a fraction of the energy that is produced by nuclear fusion, mostly deep down in its central region. There are different mechanisms that are responsible to transport this energy from the centre towards the stellar surface, we will shortly describe two of them, radiative and convective energy transport.

---

<sup>2</sup>According to Planck's law,  $B_\lambda(\lambda, T) = \frac{2hc^2}{\lambda^5} \frac{1}{e^{hc/(\lambda k_B T)} - 1}$ , in terms of wavelength  $\lambda$ . The peak in intensity  $B$  corresponds to a certain wavelength which gives the observed object its colour.

### 1.2.1 Radiative Energy Transport

If the temperature gradient is described by the Eddington equation for radiative transfer

$$\frac{dT}{dr} = -\frac{3}{4} \frac{\kappa \rho}{acT^3} \frac{L_r}{4\pi r^2}, \quad (13)$$

where  $a$  is the radiation density constant with  $ac = 4\sigma_{SB}$ , according to Lamers et al (2017), energy is transported radiatively. Photons form a gas with energy density  $u_r$  and thermal capacity  $C_r$

$$u_r = aT^4 \text{ and } C_r \frac{du_r}{dT} = 4aT^3, \quad (14)$$

as shown in Phillips (1994). The heat flux density, which is the rate of energy transfer through a unit area, then is

$$j(x) = -K_r \frac{dT}{dx}, \quad (15)$$

where  $K_r = \frac{4}{3}c\bar{l}aT^3$  is the coefficient of thermal conduction, and  $\bar{l}$  the mean free path. On their way out from the centre of a star to the surface, photons get scattered. Depending on temperature, there are different scattering processes. Discussing all of them is out of scope of this thesis, we will only sketch one case, Thomson scattering. This scattering process is dominated by photons that are elastically scattered from free electrons. The Thomson cross section is

$$\sigma_T = \frac{8\pi}{3} \left( \frac{e^2}{m_e c^2} \right)^2 = 6.652 \times 10^{-25} \text{ cm}^2, \quad (16)$$

where  $m_e$  and  $e$  are the mass and charge of the electron. According to Guidry (2019), this is valid for a gas in thermal equilibrium if  $kT \ll m_e c^2$ , which is the case for  $T \ll 6 \times 10^9$  K. Replacing now  $\bar{l}$  with

$$\bar{l} = \frac{1}{n_e \sigma_T}, \quad (17)$$

with electron number density  $n_e$  and plugging this into the expression for  $K_r$  we obtain an approximation for the heat flux density (15). Each scattering event during this random walk reduces the photon energy, until it reaches the photosphere and a part of the energy is transported to the surface.

### 1.2.2 Convective Energy Transport

According to the Schwarzschild criterion (Schwarzschild 1906), energy transport is convective if the radiative temperature gradient is larger than the adiabatic one, and radiative otherwise. This explains the condition in (6). The conditions for the Schwarzschild criterion are that a bubble of gas that is in equilibrium in pressure and composition with the surrounding medium. To describe the motion of such a bubble we closely follow the very instructive description in Lamers et al (2017). Assume that this bubble moves from a point where the surrounding medium has temperature, pressure, and density  $T_s(r_1)$ ,  $P_s(r_1)$ , and  $\rho_s(r_1)$  to a point in outward direction where the surrounding gas conditions are  $T_s(r_2)$ ,  $P_s(r_2)$ , and  $\rho_s(r_2)$ . We assume pressure equilibrium between bubble (subscript  $b$ ) and surrounding (subscript  $s$ ), meaning the bubble does neither expand, nor contract,

$$P_b(r_2) = P_s(r_2) \Leftrightarrow T_b(r_2)\rho_b(r_2) = T_s(r_2)\rho_s(r_2). \quad (18)$$

The bubble will keep rising if convection is still possible, which is, according to Phillips (1994), true if the surrounding gas is denser than the bubble Then

$$\delta\rho < \Delta\rho \Leftrightarrow \frac{1}{\gamma} \frac{\delta P}{P} < \frac{\Delta P}{P} - \frac{\Delta T}{T}, \quad (19)$$

where  $\delta$  means changes inside the bubble, e.g.  $\rho_b(r_2) - \rho_b(r_1)$ , and  $\Delta$  differences between two points in the surrounding gas, e.g.  $P_s(r_2) - P_s(r_1)$ , and  $\gamma$  is the adiabatic index. In the opposite case, if the bubble is denser than its surrounding medium, it would sink towards the centre. Schwarzschild already noted that a star could have outer shells where energy is transported radiatively, and regions deeper inside where convective zones transport energy from the source (in core regions) to layers that are further away from the centre.

If the composition of the surrounding gas is not homogeneous, Ledoux (1947) derived another criterion for convection, which can conveniently be written as (see Lamers et al. 2017):

$$-\left(\frac{d \ln(T)}{dr}\right)_b > -\left(\frac{d \ln(T)}{dr}\right)_s + \left(\frac{d \ln(\mu)}{dr}\right)_s, \quad (20)$$

where  $\mu$  is the mean molecular weight. In case of a vanishing composition gradient, (20) is the same as the Schwarzschild criterion. We will not go into more detail because this is out of scope, further information can be found in the indicated literature.

## 1.3 Stellar Evolution

We will only briefly outline the evolutionary stages of a star that are relevant in this thesis, without going into the details of rotation, turbulence, or magnetism to name a few. There is a lot of literature on the topic of star formation and evolution, the sources of this section are mainly Larson (2003), Christensen-Dalsgaard (2008), and Mo et al. (2010).

### 1.3.1 Pre Main-Sequence

As a cloud of interstellar gas accretes more and more material, at some point it will collapse under its own gravity, first noticed by Jeans & Darwin (1902). The critical mass depending on the size of a gas cloud is called the *Jeans mass* (see appendix A for a simplified derivation). When the collapse starts because of the mass exceeding  $M_J$ , it is assumed that there is a molecular core with typical density of  $\rho \sim 10^{-19} \text{ gcm}^{-3}$  and a typical temperature of  $T \approx 10 \text{ K}$  (Larson 2003, Mo et al. 2010). During this process potential energy is released. At the beginning the temperature stays roughly constant because the released energy is effectively dissipated by dust grains, while the cloud is transparent to infrared radiation. When the density reaches  $\rho \sim 10^{-13} \text{ gcm}^{-3}$  (Larson 2003, Mo et al. 2010) it is too high for the infrared photons to exit, the cloud then is not transparent to them anymore. Therefore, the energy released by the collapse can now heat the gas effectively to higher temperatures. Because the luminosity is roughly constant during this period, one can also directly see from (12) that the temperature must increase as the radius decreases.

Gas pressure, which increases rapidly as the gas heats up, now becomes significant and slows down the contraction. The core grows by accretion of gas, and the increasing mass causes a continuous contraction. Due to the increase in mass the temperature, especially in the core regions, increases until at  $\sim 10^6 \text{ K}$  the minimum for hydrogen fusion to start is reached. At that point of evolution stars are called to lie on the birthline of the Hertzsprung-Russell diagram (HRD), first noticed by Stahler (1983). The HRD plays an

important role in stellar astrophysics, especially in section 3 of this thesis where it will be explained in more detail.

### 1.3.2 Main-Sequence

When H-fusion has become efficient in the core, the new born star is said to lie on the Main-Sequence (MS) where it spends most of its active lifetime. How long this will be mainly depends on the stellar mass. The general procedure during the MS is the same for all stars, hydrogen is fused into helium in the core region,

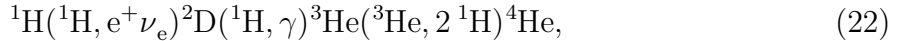


Very low mass stars with  $M_* = 0.1 M_\odot$  convert almost all of their H into He on the MS which is a lot more compared to a  $1 M_\odot$  star that only converts  $\approx 10\%$  of its total amount of H during this phase, according to Adams et al. (2005). As a result, both the  $M_* = 0.1 M_\odot$  and  $M_* = 1 M_\odot$  stars have a comparable amount of fuel that can be used on the MS. But since the temperature of an M dwarf <sup>3</sup> is lower, fusion processes are less efficient and therefore, the less massive star stays longer on the MS.

The two possible reactions that fuse H into He are the pp chain and the CNO cycle.

#### pp chain

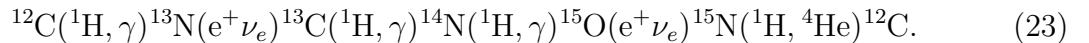
One example for the pp chain is the pp-I reaction, which is also the dominant one:



where the positron and the neutrino originate from a  $\beta^+$  decay. Since in this process two  ${}^3\text{He}$  are needed, the first two reactions have to take place twice (Maeder 2009). Because the conversion from a proton to a neutron involves a weak reaction, it has an extremely small cross section factor and therefore is the slowest reaction which determines the efficiency of the pp chain (Christensen-Dalsgaard 2008).

#### CNO cycle

This process needs several metals acting as catalysts to take place. It is called cycle because at the beginning and the end there is a  ${}^{12}\text{C}$  nucleon needed for the reactions. Furthermore, there are several proton ( ${}^1\text{H}$ ) captures and  $\beta^+$  decays.



Here the  ${}^{14}\text{N}({}^1\text{H}, \gamma){}^{15}\text{O}$  has the smallest interaction rate, so this is the reaction that determines the efficiency of the CNO cycle (Christensen-Dalsgaard 2008).

The energy rates per unit mass  $\varepsilon$  of both reactions depend on temperature, mainly determined by the stellar mass. The pp chain dominates at lower temperatures,  $T \approx 15 \times 10^6$  K where  $\varepsilon_{pp} \propto T^4$ , whereas the CNO cycle dominates at  $T \approx 20 \times 10^6$  where  $\varepsilon_{CNO} \propto T^{17-20}$ , as explained in Aguirre (2017), and Karakas (2017). Therefore, energy production is dominated by the pp chain for stars  $\lesssim 1.25 M_\odot$ , and the CNO cycle for more massive stars.

---

<sup>3</sup>According to the Harvard spectral classification, see also section 3.

### 1.3.3 Late-time Evolution

Since the evolutionary stages after the MS strongly depend on stellar mass, we discuss them separately by mass range. The differentiation in literature is not very consistent, so we will define it as follows: Low mass stars have masses below  $\approx 0.25 M_{\odot}$  which is, according to Laughlin et al. (1997), the minimum mass needed to become a red giant (RG). Intermediate mass stars have a core that will not become hot enough to start carbon fusion. The minimum mass for this reaction to start is roughly  $10 M_{\odot}$ , see for example Iben (1985), Nomoto et al. (2013), and Karakas (2017) who have slightly different values. We adopt the limit such that the intermediate mass stars are the ones in the range  $0.25 M_{\odot} \leq M_* \lesssim 10 M_{\odot}$ . Stars with masses above  $\approx 10 M_{\odot}$  are considered to be massive stars.

#### Low mass stars

The lowest mass stars, the M dwarfs or red dwarfs, have a mass of up to  $\approx 0.5 M_{\odot}$ . Therefore, only a part of them is considered to be low mass stars in our classification. For example a  $0.10 M_{\odot}$  star, as described in Laughlin et al. (1997), that undergoes a period of shell-burning where H is converted to He not in the core region but in an outer shell, will become hotter than the Sun whereas the luminosity is only  $\sim 0.01 L_{\odot}$  (blue dwarfs). It will then cool down, finally ending up as a white dwarf (WD). These are very dense objects where the pressure that supports the star does not come from radiation, but from degenerate electron gas pressure (all quantum states are filled up to the Fermi energy). They have a low luminosity,  $L \sim (10^{-4} - 10^{-1})L_{\odot}$  but surface temperatures of  $T \simeq (6000 - 2 \times 10^4)$  K, so their radii have to be small ( $R \simeq 10^9$  cm), according to Rose (1998). Since WD do not fuse hydrogen anymore, they only emit thermal radiation. As a consequence they become fainter and colder with time. Low mass stars can have lifetimes of several trillions of years (Laughlin et al. 1997, Adams et al. 2005). With stellar lifetime, we mean the time a star maintains nuclear fusion processes.

#### Intermediate mass stars

The luminosity of a star increases with time, see appendix C, so according to (12) there are two possibilities for a star to stay stable. It can either become hotter or larger. As discussed before red dwarfs increase their temperature, but for more massive stars the behaviour is different. As temperature increases, opacity increases a lot. Therefore,  $T_{\text{eff}}$  stays nearly constant forcing the star to expand (Adams et al. 2005). At the same time core H-fusion ceases (Aguirre 2017). Due to the missing energy production in the core,  $T_{\text{eff}}$  decreases but  $L$  stays more or less constant, and  $R$  increases. This evolutionary phase takes place on the so-called subgiant branch (Hurley et al. 2000). As H is converted into He in the shell, the star increases in size, and becomes a RG. Due to core contraction  $T_c$  rises because of the virial theorem (appendix B) until it is high enough to ignite core He fusion at  $\simeq 10^8$  K (Rose 1998). In this phase He is converted to heavier elements, mostly Carbon and Oxygen. There are two different ways how He fusion starts, depending on stellar mass.

$\lesssim 2.2 M_{\odot}$

As described in El Eid (2018) electrons are degenerate in the core after core H fusion ended. Shell H fusion proceeds, heating up the core, where thermal energy is independent of temperature due to electron degeneracy. When He fusion starts, temperature increases locally but because of degeneracy, pressure does not increase. The higher temperature causes higher reaction rates, increasing temperature even more. At some point thermal pressure removes degeneracy, as summarised by Aguirre

(2017). According to Karakas (2017), and Christensen-Dalsgaard (2008), the phase of this so-called He flash lasts only for some hours. In this time, 3% of all core  $^4\text{He}$  is converted into  $^{12}\text{C}$  and core luminosity reaches up to  $10^{11}L_\odot$ . The core then is not degenerate anymore and proceeds with smooth He fusion. Radiation pressure becomes higher, the core can expand and cool until equilibrium is reached.

$\gtrsim 2.2M_\odot$  Because of the convective core (see section 1.2.2) elements in this region are well mixed, resulting in a more or less homogeneous core. This means that when there is no more H at the centre, it disappears in the entire core region. The He core contracts and heats until triple alpha reactions start He fusion<sup>4</sup> (Iben 2012).

The process then kind of repeats with running out of fuel for core He-fusion, resulting in a star with a core of heavy elements and two burning shells consisting of H and He. On the so-called asymptotic giant branch the star undergoes a period of thermal pulses caused by a series of ignition and extinction of He shell burning. During this phase heavy elements can be produced via neutron capture. Due to these pulses the star loses most of its mass, except the hot core. What is left in the end is a WD, probably surrounded by a planetary nebula (El Eid 2018, Aguirre 2017). Intermediate mass stars stay on the main sequence for about 30 Myr ( $8 M_\odot$ ) to 10 Gyr ( $1 M_\odot$ ) and have a total lifetime of approximately 36 Myr to 12 Gyr, respectively (Karakas 2017).

## Massive stars

The most massive stars evolve like the intermediate mass stars without degenerate core up to shell He-burning, but without thermal pulsation. Due to its mass the core region becomes hot enough to ignite carbon-fusion ( $T \sim 5 \times 10^8$  K), where  $^{12}\text{C}$  is converted to magnesium, sodium, neon, and oxygen. At the end of core C-fusion, the procedure is again similar to what happened before, with a star consisting of a core made of the elements fused in C-fusion and now three shells consisting of H, He, and C. Depending on the stellar mass, heavier elements such as  $^{20}\text{Ne}$ ,  $^{16}\text{O}$  are fused one after another at around  $10^9$  K. At these high temperatures, heavy nuclei can capture  $\alpha$  particles ( $^4\text{He}$ ), creating heavier elements up to  $^{52}\text{Fe} + ^4\text{He} = ^{56}\text{Ni} + \gamma$ , as outlined in Christensen-Dalsgaard (2008). These processes are referred to as silicon burning. The mean binding energy per nucleon starts to decrease with increasing mass number and fusion is not energetically favourable anymore at this point. The star is now built up like an onion with many shells of different elements. It then has no more fuel to stay in thermal equilibrium, the core collapses and causes a type II supernova, ending up in a neutron star or a black hole. But since these stages are out of scale covered by the diagrams in section 3, we do not go into further detail. Because the most massive stars are very efficient in fusion processes they have significantly shorter lifetimes. For example a  $60 M_\odot$  star lives only for about 4 Myr (Yungelson et al. 2008). Furthermore, the heavier the elements become that are involved in the fusion processes, the shorter these stages last. Oxygen and Silicon burning only sustain for months or even days, instructively illustrated in Bethe & Brown (1985).

---

<sup>4</sup>Two  $^4\text{He}$  ( $= \alpha$  particles) form an unstable  $^8\text{Be}$  which quickly captures another  $\alpha$  to form a  $^{12}\text{C}$

## 2 Methods

### 2.1 Data acquisition

The *Gaia* data can be accessed in different ways, a convenient one is to use the ADQL (Astronomical Data Query Language) in the *Gaia* archive<sup>5</sup>. One can select the desired quantities of (e.g.  $T_{\text{eff}}$ ,  $L$  and so on) from the entire data set, convert it to a suitable data format and download it. The *GES* data were accessed via *Topcat*<sup>6</sup> (Tool for OPerations on Catalogues And Tables) which was also used to do the crossmatch between the two catalogues. This was necessary because some quantities, such as  $R$  or  $g$ , did only appear in one of the data sets, and we had to assign these quantities to the correct star in the other set. Some quantities are provided in logarithmic scale with base 10, everywhere where we write log we mean  $\log_{10}$ . The individual masses were derived using the given surface gravities and radii,

$$M = \frac{gR^2}{G}. \quad (24)$$

To have the masses in solar units, like the measured radii, the result had to be divided by  $g_{\odot} = 274 \text{ ms}^{-2}$ <sup>7</sup>. The crossmatch contains measurements of 7962 stars. To increase the quality of the studied objects only those with uncertainties less than 5% of the measured temperature, surface gravity, and radius were considered, which was satisfied by 6797 stars.

Table 1: Data statistics

	min	mean	median	max
$T_{\text{eff}}$ [K]	3483	5330	5321	7549
$L/L_{\odot}$	0.041	8.087	1.32	288.5
$R/R_{\odot}$	0.506	3.039	1.227	30.30
$g$ [ $\text{ms}^{-2}$ ]	0.299	196	176	1590
$M/M_{\odot}$	0.009	1.23	0.97	68.5
$Z/Z_{\odot}$	-2.13	-0.11	-0.066	0.61

In this table, as well as in figure 1, we see from the mean that many stars have  $T_{\text{eff}}$  slightly below  $T_{\text{eff},\odot}$ ,  $R$ , and  $L$  are larger than solar values but with significantly lower surface gravity.

<sup>5</sup><https://gea.esac.esa.int/archive/>

<sup>6</sup><http://www.star.bris.ac.uk/~mbt/topcat/>

<sup>7</sup>NASA Sun fact sheet, <https://nssdc.gsfc.nasa.gov/planetary/factsheet/sunfact.html>

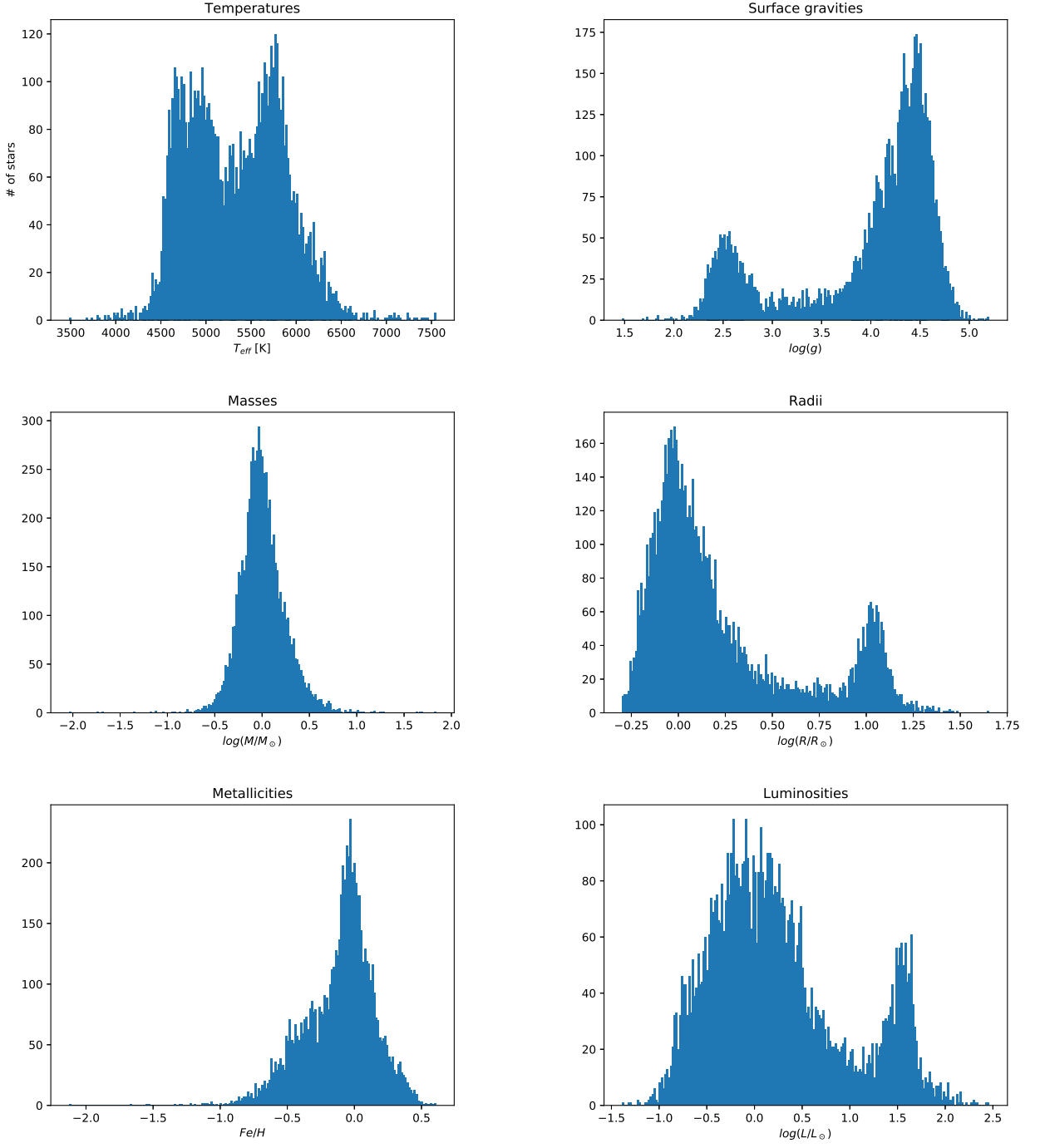


Figure 1: We see already that many of the observed stars have properties within an order of magnitude compared to the Sun. There are only 18, 26, and 172 stars above  $10 M_{\odot}$ ,  $20 R_{\odot}$ , and  $50 L_{\odot}$ , respectively.

What can already be seen in figure 1 is that there are large objects, some with comparably low density, and some with high luminosity. Furthermore, there are two distinct peaks in  $T_{\text{eff}}$ . Only by looking at these figures we cannot say if the different peaks in one histogram are related to the peaks that can be found in other histograms. But we know that RG would be candidates that match criteria of one of those peaks. We will see in section 3 if it is possible to identify two different groups of stars, and if one of them indeed is the RG. From table 1 we see that there is a great variety in the different observed quantities.

## 2.2 Friends of Friends

A Friends of Friends (FoF) algorithm is very useful to find objects with similar properties in a large data set. Normally the particles, in our case the single stars, are considered in a defined space, for example the phase space. A first data point is selected and the distance between this point and all the other data points has to be calculated. If a point is closer than a predefined linking length (LL), this point is considered as a friend of the first point. All these points within a certain distance are assigned to a first group. Then, the distance between a first point in this group to all other points in the data set which are not yet in this group is calculated. If a point is closer to this friend than the LL, it is considered as friend of this friend. All these friends of friends are added to the initial group, representing the first group that was found, and all objects in this group are not considered in the algorithm anymore. Then, one of the remaining points is selected and the procedure repeats until there is no object remaining.

To find stars with similar properties, the considered space was, according to our new diagram that will be introduced in section 3.2, the four dimensional  $T_{\text{eff}} - M - R - Fe/H$  space. Since the metallicity  $Fe/H$  (or  $Z$ ) is a logarithmic quantity

$$Fe/H = \log_{10} \left( \frac{N_{Fe}}{N_H} \right)_{\text{star}} - \log_{10} \left( \frac{N_{Fe}}{N_H} \right)_{\odot}, \quad (25)$$

where  $N$  is the respective number of atoms per unit volume, not  $Fe/H$  was considered, but  $10^{Fe/H}$ . Now,  $Fe/H$ ,  $M$ , and  $R$  are given in dimensions of solar units. Therefore,  $T_{\text{eff}}$  has to be divided by  $T_{\odot, \text{eff}} = 5778$  K. This makes the contributions of all the quantities more comparable such that the LL is a meaningful measure to find groups. The distance between two stars is calculated with an Euclidean metric,

$$ds_j = \sqrt{(M_i - M_j)^2 + (R_i - R_j)^2 + (T_{\text{eff}, i} - T_{\text{eff}, j})^2 + (10^{Fe/H_i} - 10^{Fe/H_j})^2}, \quad (26)$$

where  $i$  stands for the selected object the distance is calculated from and  $j$  for each considered object. Because there is a relatively wide variety in  $R$ , the radius can dominate this distance by far. This should not cause a big problem because in the observed data are no objects at the upper end of the MS, so these stars are really supposed to be RG. Therefore, if the term  $(R_i - R_j)^2$  is large, the two compared objects probably have not very much in common. The value for LL can in principle be chosen arbitrarily. A value that is too small would lead to no result because most objects exceed the limit. On the other hand, if LL is too large, most of the stars would be within this distance resulting in one big group, which has no meaning.

## 2.3 Evolutionary Tracks

The Modules for Experiments in Stellar Astrophysics (*MESA*<sup>8</sup>) library (Paxton et al. 2011, 2013, 2015) is an open source program consisting of several modules. As a star evolves, mass loss or accretion, nuclear reactions, and time itself influence (1)-(5). All this is taken into account, together with a created nuclear reaction network and several inputs, such as a suitable equation of state (EoS). A single evolutionary track shows the evolution of a star with certain initial mass  $M_{\text{ini}}$ , and chemical composition. We will not go into details of how these evolutionary tracks are calculated, extensive description can be found in the references.

---

<sup>8</sup><http://mesa.sourceforge.net>

## 2.4 Isochrones

The used data for the isochrones in this thesis are taken from the MESA Isochrones & Stellar Tracks (*MIST*<sup>9</sup>) project (Dotter 2016, Choi et al. 2016, 2017). Starting with the information of many evolutionary tracks from *MESA*, different points on an isochrone represent stars with same initial composition but different  $M_{\text{ini}}$  at a fixed age. The assumption is that all these stars have formed at the same time from a homogeneous gas cloud (Dotter 2016, where the principle of how isochrones are constructed is described in detail). The evolutionary tracks on which the used isochrones are based on contain information of stars with masses of  $(0.1 - 300) M_{\odot}$  and the isochrones cover a range of  $\log(\text{age}) = 5$  to  $\log(\text{age}) = 10.3$ . Further description of the used set of isochrones can be found in Choi et al. (2016).

---

<sup>9</sup><http://waps.cfa.harvard.edu/MIST/>

### 3 Diagrams in Stellar Astrophysics

Mankind has been looking at the stars for centuries, and with time, started to measure different physical quantities of these peculiar objects. Science and technology have become more and more capable of observing quantities that were not possible in the previous centuries or even decades, and the precision of measurements increased significantly. To understand observational results and make connections visible, one can plot different quantities that are measured against each other. Of course, there are some combinations that are more meaningful than other ones. In this chapter we will first explain the HRD, and then introduce our new three-dimensional diagram.

#### 3.1 The Hertzsprung-Russell Diagram

Probably the most famous diagram in stellar astrophysics was first suggested at the beginning of last century independently by Ejnar Hertzsprung, and Henry Norris Russell. Hertzsprung (1908) wondered if small differences in spectra of stars go along with large changes of the absolute magnitude<sup>10</sup>. He also mentioned in the same paper, that there is a correlation between colour and temperature. Such a comparison was first published by Hans Rosenberg (1910) who was in correspondence with Hertzsprung, with the width of different spectral lines instead of the spectral class on the x-axis. With much more data a similar diagram (figure 2) was published by Russell (1914). He already saw that there are two prominent lines, a diagonal which later was recognised to be the MS and a horizontal one, the giant branch (GB).

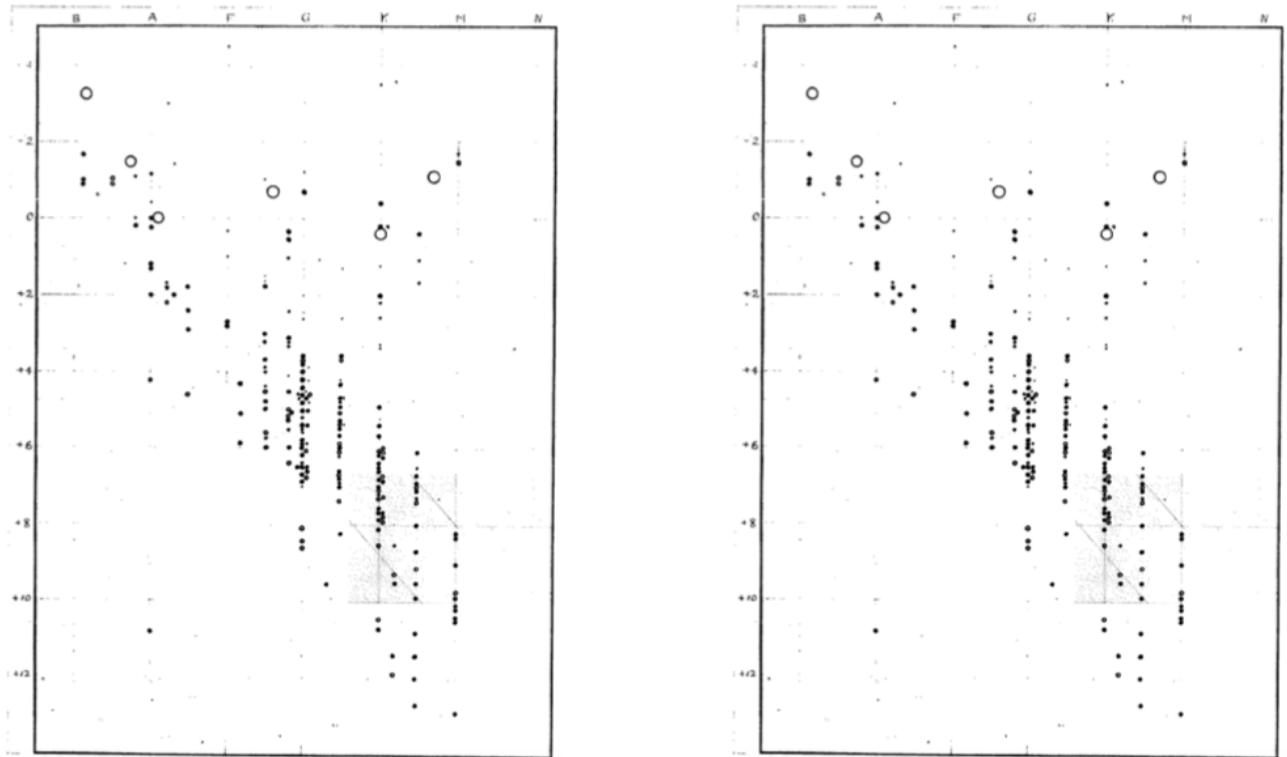


Figure 2: The first diagrams that are now known as HR diagram, published by Russell (1914). Even though they only contain about 300 stars, all the important regions known from the HR diagram are already visible.

There are different versions of the original HR diagram, for example colour-magnitude

<sup>10</sup>Hertzsprung already suggested such a diagram 1905 but the sources were not accessible.

or luminosity-temperature diagrams. The HRD is very useful because the different evolutionary stages can be identified quickly, as illustrated in figure 3.

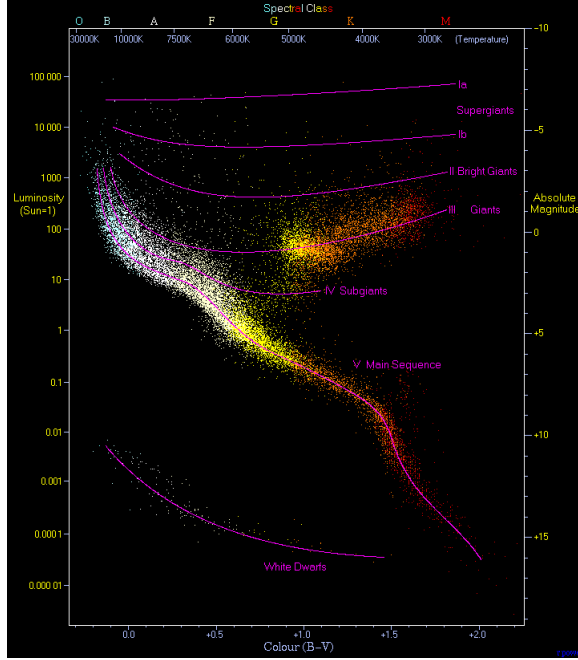


Figure 3: A version of the HRD with all labels on the x- and y-axis that have become popular during the last century.

Credit: Richard Powell, CC BY-SA 2.5, via Wikimedia Commons.

### 3.2 A New Three Dimensional Diagram

Technology improved significantly in the last century. Satellites have been invented, and ground based telescopes improved a lot, which both have shown us stars and galaxies as never seen before. For example *Gaia*<sup>11</sup> has been mapping the Milky Way to a very high accuracy. We used a combination of the *Gaia*'s second data release (DR2, Gaia Collaboration et al. 2016, Gaia Collaboration et al. 2018) and the *Gaia-ESO Survey*<sup>12 13</sup> (GES). With information about the  $T_{\text{eff}}$ ,  $L$ ,  $R$ ,  $g$ , and  $Z$  we introduce a new 3-dimensional modern version of the HR diagram with more fundamental physical quantities. Russell (1914) already mentioned the connection between spectral class and the photospheric temperature, so  $T_{\text{eff}}$  is still a good choice as a quantity in the new diagram. The luminosity, assuming the energy to be emitted as black body radiation, given by (12), depends on  $T_{\text{eff}}$  and  $R$  of the star. Since stars that differ in  $L$  are stars that have also differences in  $T_{\text{eff}}$ , at least on the MS, we decided to take the radius instead of the luminosity. This choice is convenient since the GB in the HRD is separated from the MS, so one can expect a similar behaviour not because of the higher  $L$  compared to the MS, but a larger  $R$ . As a third quantity, considering the accessible data, one could take the surface gravity  $g$  or the mass derived from  $g$  and  $R$ . Assuming a star keeps constant mass during its evolution from the MS to the giant branch (of course this is not true in general), the surface gravity changes a lot. This makes differences more obvious in a diagram, as shown in figure 4. This is important because the diagram presented here should illustrate the evolutionary stages of stars at least as conveniently recognisable as the HRD. On the other hand, mass

<sup>11</sup><https://sci.esa.int/web/gaia>

<sup>12</sup><http://ges.roe.ac.uk>

<sup>13</sup>Based on data products from observations made with ESO Telescopes at the La Silla Paranal Observatory under programme ID 188.B-3002.

is a more fundamental quantity. According to the Vogt-Russell theorem after Vogt (1926), and Russell et al. (1927)<sup>14</sup>, with a proof given in Chandrasekhar (1939), properties at the stellar surface are determined only by the mass and the chemical composition, if  $\kappa$ ,  $P$ , and the energy generation rate  $\varepsilon$  are functions of the local  $\rho$ ,  $T$ , and the chemical composition. However, as for example explained in Carroll & Ostlie (2017) rotation and magnetic fields also play minor roles in stellar evolution. At the same place, Carroll & Ostlie (2017) suggest not to call it a theorem, but a general rule.

One could argue that uncertainties would be much more correlated in case of the mass, especially if  $R$  is already derived from  $L$  and  $T_{\text{eff}}$ . However, if the uncertainties are not significant, this would not really have an influence in such a diagram, and  $M$  instead of  $g$  could still be a good choice. In the HRD, it is not important to show the very exact position of a single object. What is important is the region compared to other stars in a sample to identify the evolutionary stage of a star at the moment it is observed, and so it is in the 3-dimensional diagram. Therefore, it should be enough to restrict the uncertainties not to exceed some percentage, as described in section 2. Because of this we decided to select the mass as third quantity. The only advantage of the diagram with  $g$  instead of  $M$  we found would be that the stars are distributed more compactly as one can suspect from the top row of figure 4. For convenience the mass and radius axes are shown logarithmically. Note that when we refer to these quantities, and to the luminosity, in a diagram we do not mention log explicitly. Having this 3-dimensional diagram, colour can be used to introduce  $Z$  as a fourth dimension.

---

<sup>14</sup>Only the reference was found for Russell et al. (1927) but not the original paper.

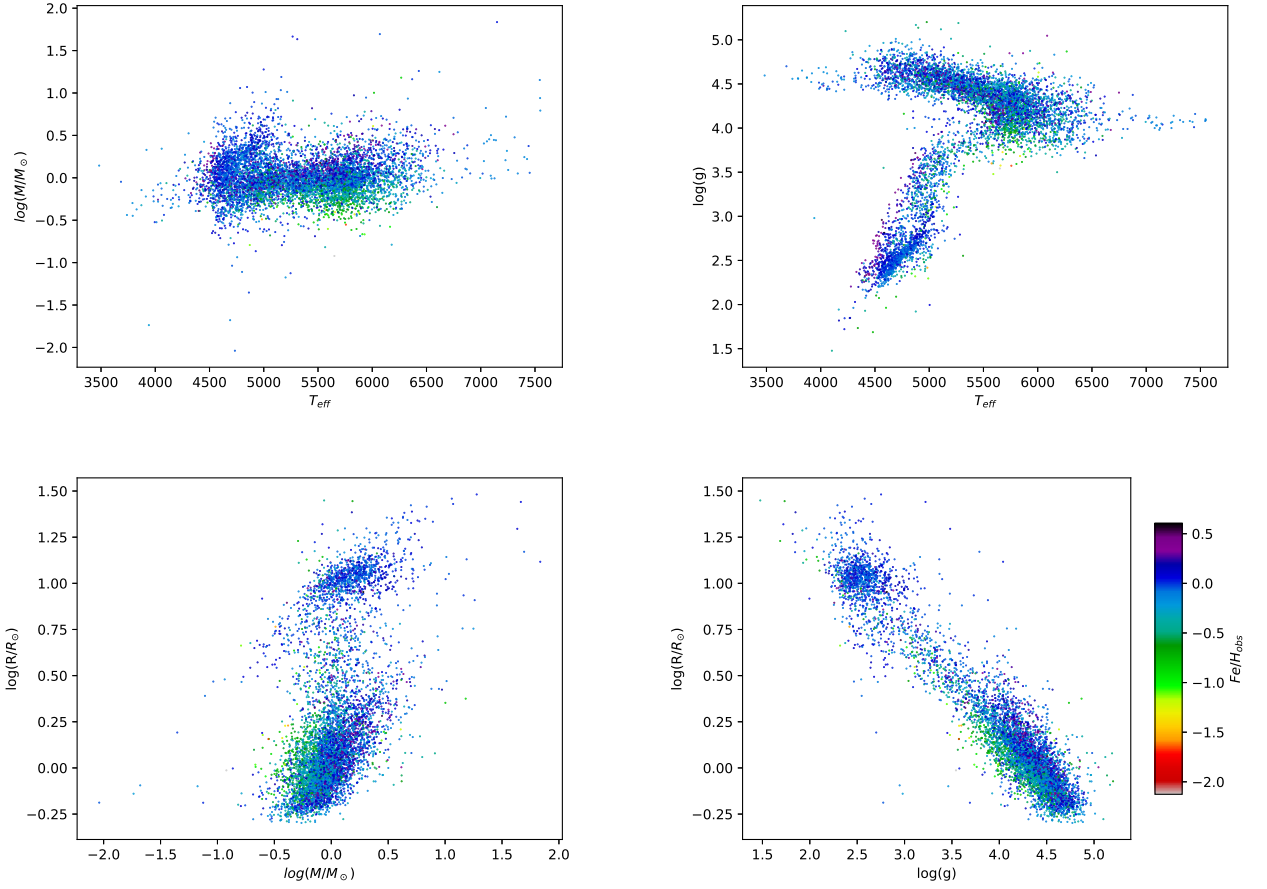


Figure 4: These plots illustrate why it would be favourable to choose  $g$  instead of  $M$ . In the top row one can see that, with mass, the distribution is more or less a big bunch with only little indication of, for example, MS and RG stars in this  $M - T$  diagram. On the other hand, these two stages in the evolution of stars can be identified much easier if one replaces  $M$  with  $g$ . The bottom line shows two distinct groups for both  $M$  and  $g$ .

### 3.3 Comparison between the Diagrams

To compare the 3-dimensional diagram with the HRD on 2-dimensional paper we show the 2-dimensional projections along with the HRD in figure 5. It is true that there is not much sense of a 3-dimensional diagram on paper. However, since a major part of research in astrophysics relies on computers, our diagram still has some benefits. For historical reasons, temperature decreases from left to right on the HRD, which is not the case in our diagram. We can see distinctive groups in both the HRD and our diagram, as can already be anticipated from the histograms in figure 1. It can also be seen from the HRD at the bottom right in figure 5 that the data contain MS stars, and some that belong to the giant branch. To verify that these distinct groups in our 2-dimensional projections are really the MS and the GB known from the HRD, a FoF algorithm as described in section 2.2 was applied to the data set. The results are shown in figure 6. As expected, the  $R - T$  projection of our diagram looks very similar to the HRD besides the reverse temperature scale.

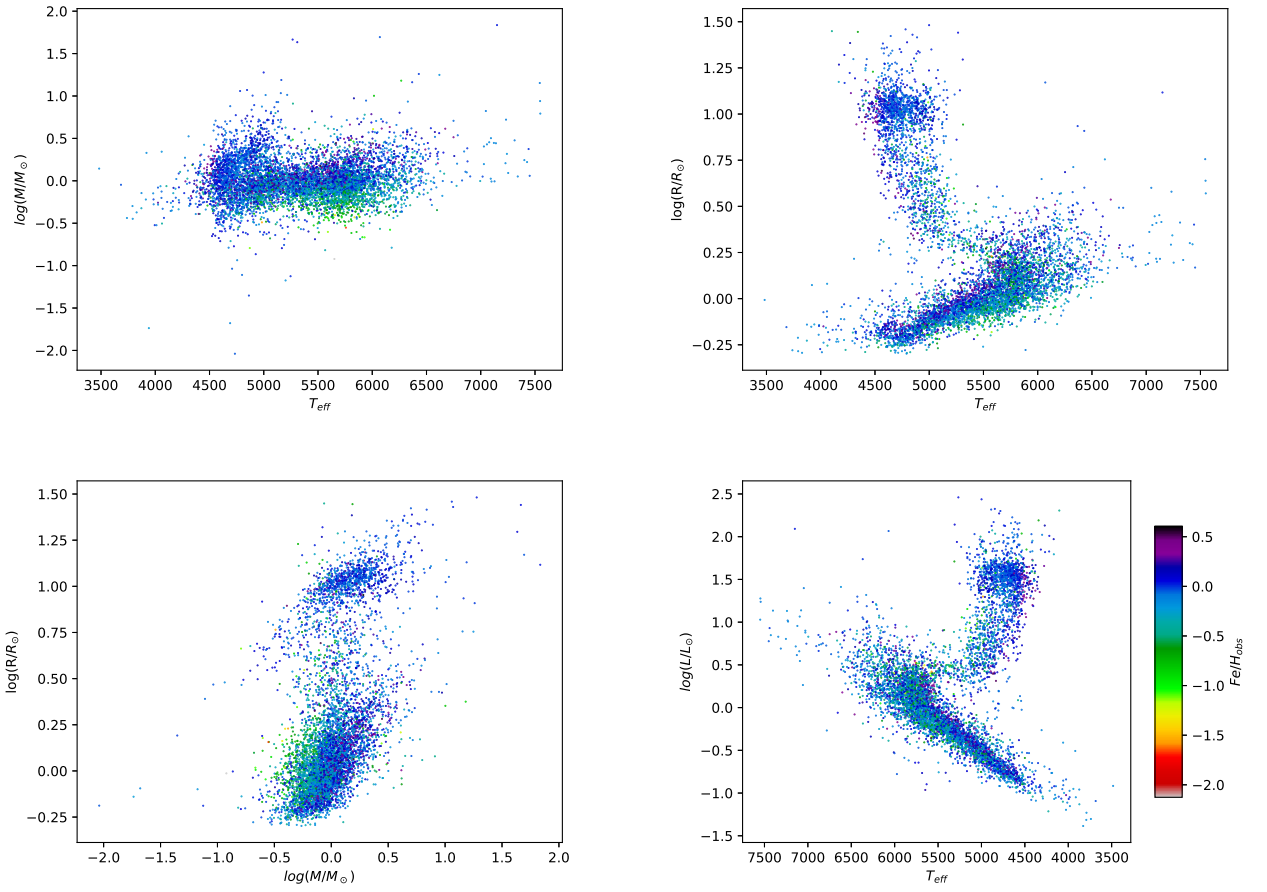


Figure 5: The top row and bottom left show the projections of our diagram, bottom right shows the HRD. The diagrams show two relatively well distinct groups, except the  $M - T_{\text{eff}}$  case. One can also see a tendency in the  $Z$  distribution indicated by colour.

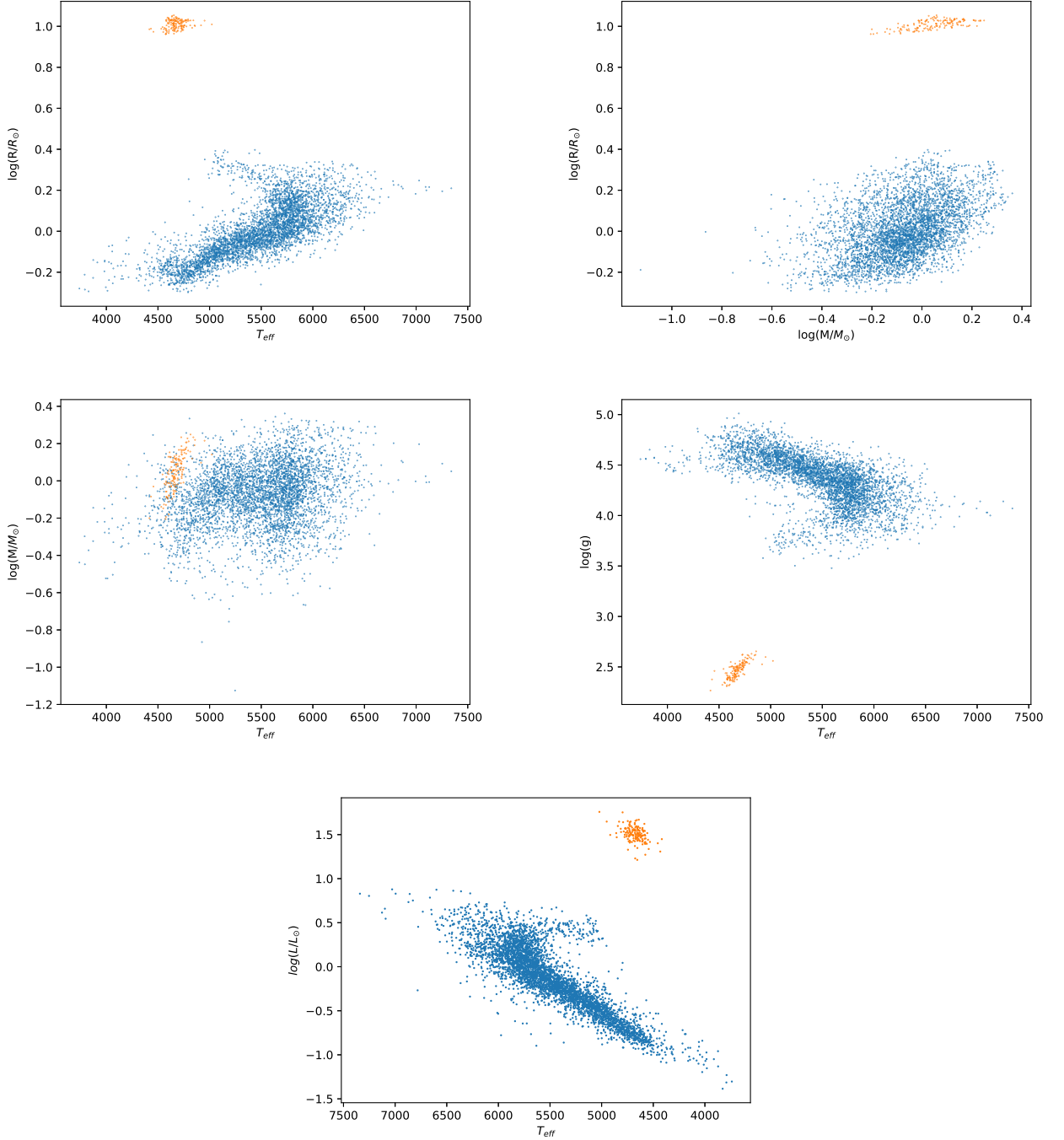


Figure 6: This figure shows the results of the FoF applied to the data set. One can see from the bottom diagram where the MS (blue) and the GB (orange) are located. The top and middle row show the locations of these groups in the projections of the 3D diagram as well as the location in the  $g - T_{\text{eff}}$  plane compared to the  $M - T_{\text{eff}}$  plane.

It is obvious from figure 6 that the FoF algorithm did not assign all stars from the data to a group. This is due to the design of the algorithm, and because only groups with at least 50 members are shown. Most of the smaller detected groups are between MS and GB (the subgiants in figure 3), or they lie in the MS or GB. It is much more likely that this effect is based on the design of the FoF rather than different initial compositions as an effect of different ages or even different origins of the individual stars. Figure 6 does not at all claim to be complete, it should only indicate the regions where these important groups of stars can be found. It is clear from figure 5 that the GB is much more extended and that

there is more scatter around the MS, which further extends to higher  $T_{\text{eff}}$  and  $L$ . One can see that the MS and GB are clearly separated in all two dimensional diagrams except in case of  $M - T$ . This is expected because all stars in the data set, besides very few ones with  $\log(M/M_{\odot}) \approx -0.6$  reach this evolutionary stage at some point. Furthermore, since, according to Meynet et al. (1993), mass loss is not significant for MS stars and subgiants in this mass range, it would make sense that RGs have still similar masses if they evolved to RG recently. If these stars had a much higher initial mass, they would probably be hotter and/or larger.

Starting from the HRD one can identify the MS and the GB without difficulty in the top row. Because the mass does not change dramatically, it is not a surprise that the giants are located in the same mass range as the MS but it can clearly be seen that the GB is at the low-temperature range of the diagram. The WD and the supergiants are not shown in this diagram because they do not appear in the *Gaia-GES* crossmatch. The MS is also not covered completely by the data. A good way to find the positions of these important evolutionary stages is to plot theoretical isochrones in both the HRD and our 2D projections of the diagram, and compare them as shown in figure 7. The evolutionary stages then can easily be located in the full 3D diagram.

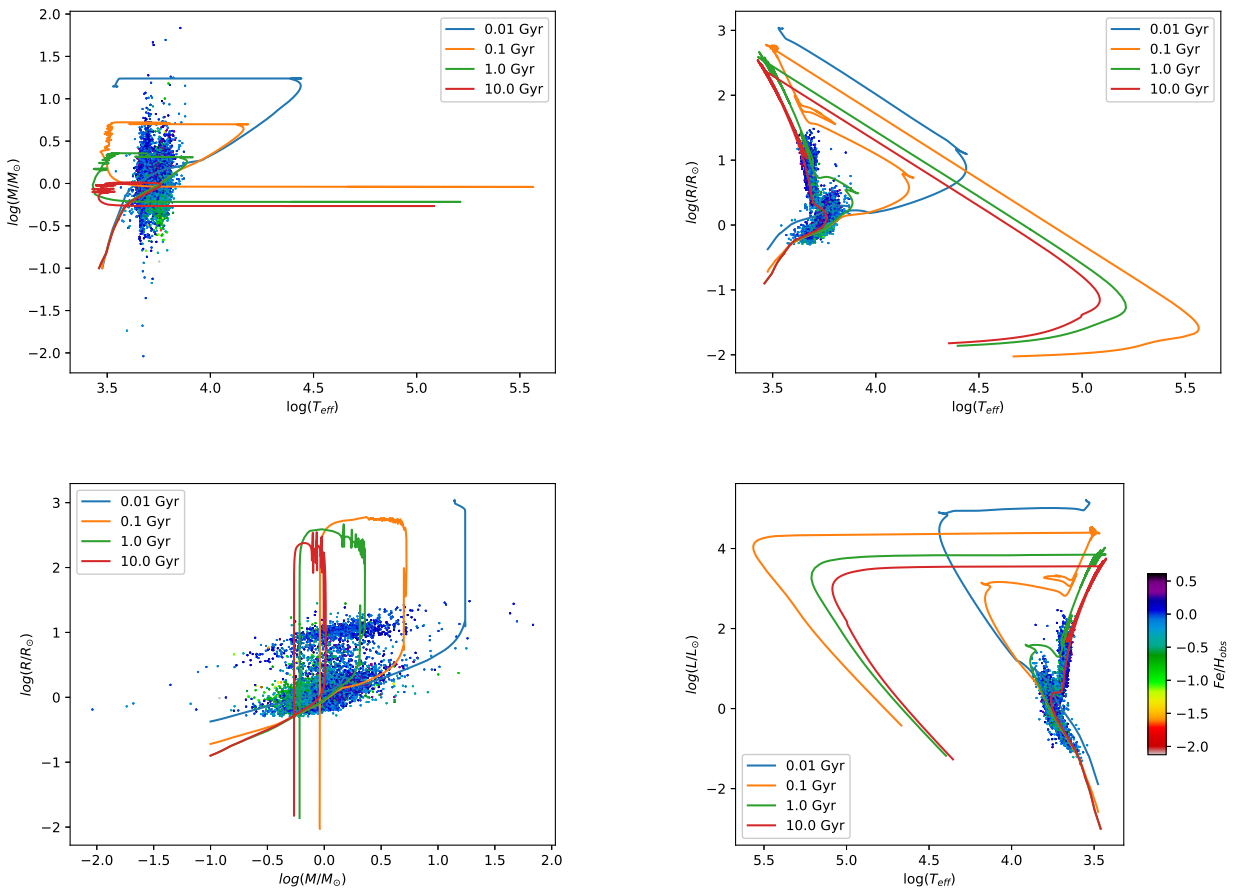


Figure 7: The isochrones show where stars with different  $M_{\text{ini}}$  are located in the HRD (bottom right) at a fixed time. Note that in the  $M - T$  diagram (top left) the final temperature is not at the high- $T$  end but it cools down keeping  $M$  approximately constant, see appendix D.

Starting from the HRD (bottom right) the 10 Myr (blue) and the 0.1 Gyr (orange) isochrones show an extension of the MS to more massive stars. Those on the 10 Myr isochrone leave the MS around  $\log(T_{\text{eff}}) = 4.45$  which is roughly 30'000 K. The following

horizontal line then represents the supergiants. Due to its characteristic end point and the hook<sup>15</sup> at the end of the MS, it can easily be identified in the other diagrams. The end points of the 0.1 (orange), 1 (green), and 10 (red) Gyr show the region where the WD are located. Of course, they cool to much lower temperatures but this is not covered by the model anymore. Radius and mass will stay almost constant during this last cooling phase, so one can guess the region where they would be located in the end. From the  $R - M$  diagram it seems that WDs become smaller and smaller with time but this is not the case as one can verify by looking at the two top row diagrams in figure 7.

---

<sup>15</sup>At the end of the MS, due to convection, there is an extended region without H. Therefore, the core contracts rapidly (Pols et al. 1998). If there is no convective core, as in stars with lower masses, there is no hook as one can see from the red isochrone of the HRD in figure 7.

## 4 Age Determination

### 4.1 Procedure

One possibility to estimate the age of a star is to find the theoretical isochrone that matches the observed data best, as already mentioned by Meynet et al. (1993). However, as summarized in Soderblom (2010), this method has also some disadvantages. In a first step we want to find the theoretical point from each isochrone which is closest to a specific star, somewhat similar to the first loop of the FoF described in 2.2. Because the isochrones are grouped by metallicity, the first thing to do is to select the set of isochrones with theoretical metallicity closest to the measured one of the star. Then, for each isochrone with this metallicity the distances between theoretical values and observed data in  $T_{\text{eff}}$ ,  $g$ , and  $r$  are determined. Similar to (26) the distance is calculated:

$$ds = \sqrt{\left(\frac{T_{\text{obs}} - T_{\text{th}}}{\Delta T_{\text{obs}}}\right)^2 + \left(\frac{R_{\text{obs}} - R_{\text{th}}}{\Delta R_{\text{obs}}}\right)^2 + \left(\frac{g_{\text{obs}} - g_{\text{th}}}{\Delta g_{\text{obs}}}\right)^2}, \quad (27)$$

where  $\Delta$  is the respective uncertainty on observational data. In addition to the limitation of uncertainties not to exceed 5% of the measured values, they are considered here to have a qualitative weight between observed and theoretical data. Because the isochrones only were available for some  $Z$  as described before, the uncertainties on the observed  $Z$  were omitted due to their negligible influence. For each isochrone the closest value is then stored in a list. After going over all isochrones the object in this list which is closest to the star gives the estimated age. However, there are some caveats. As mentioned in Soderblom (2010), different isochrones can cross the same point on the HRD. It is therefore important to be able to know the chemical abundances quite well to tell which isochrone estimates the star's age best. Since we only approximate the real abundances with the ones provided by the theoretical data, this can have a large influence. The limitations due to uncertainties that are also mentioned by Soderblom (2010) are probably less significant in our case due to the good accuracy of the available data, but they still have to be considered. Another limitation that has some major influence is the choice of the lower and upper boundary of the ages as well as the time steps. Of course, the upper boundary is given by the age of the universe. The lower limit was randomly chosen to be 1 Gyr, and the time steps are also 1 Gyr, where this limitation was set by the computation power and a reasonable running time. These calculations were executed parallel using the multiprocessing module in python.

### 4.2 Age estimation

Comparing these results with the stellar properties in figure 1, this is probably not something one would expect. Many stars have properties that are comparable to solar values, but most ages are far away from the Sun's age. Therefore, it would be interesting where the stars with different ages are located both in our and in the HR diagram, and if there is a real correlation between location and age.

It seems that our approach does, as expected, not provide a sufficient estimate of stellar ages for many stars. However, when the stars are plotted with a colour code not for metallicity but for age, an interesting effect as can be seen in figure 10 occurs. It seems that the less massive stars are generally older than the more massive ones, which can be expected because stellar lifetime decreases a lot with increasing mass as seen in section 1. This effect of separation is not present in the MS part of the  $R - T$  subplot and the

HRD (figure 10 top left and bottom right, respectively), and it is also not very clear for the subgiants and the RG in these two cases.

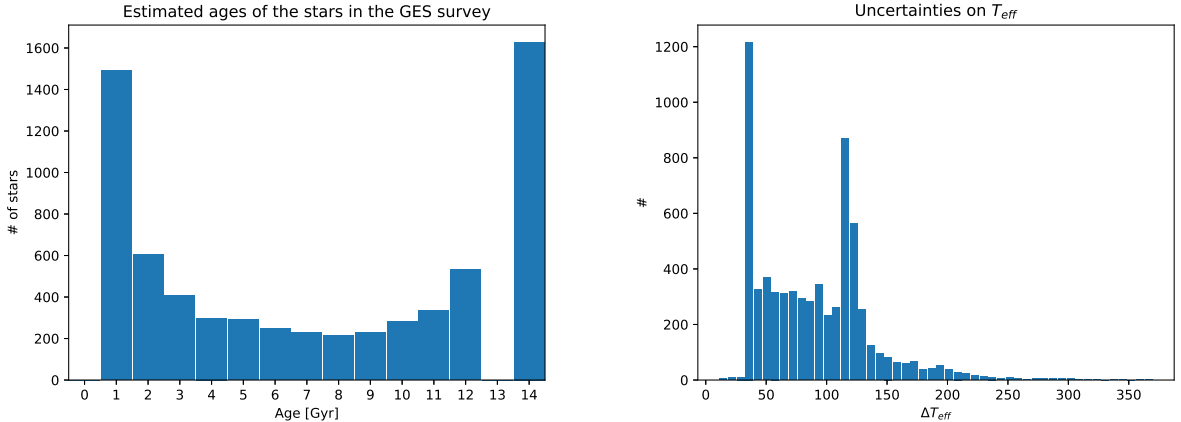


Figure 8: One can see that the age estimate gives a result which would not be expected from, for example, the stellar masses in the data.

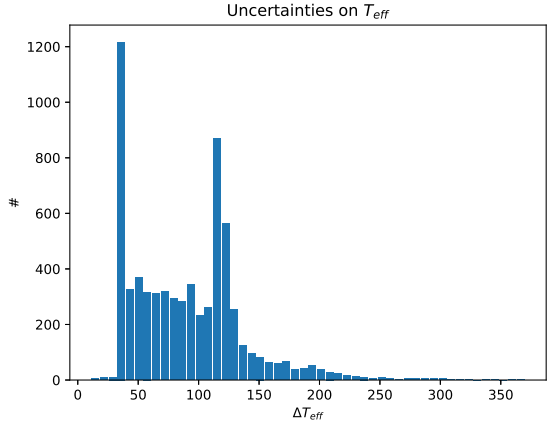


Figure 9: It seems that there is a lower threshold of the uncertainties, with only very few stars with an uncertainty below 36 K, and a second peak at  $\approx 115$  K.

Table 2: Estimated ages

Age [Gyr]	#
1	1493
2	606
3	409
4	299
5	293
6	247
7	227
8	214
9	229
10	283
11	337
12	531
14	1629

This table shows the number of stars contained in each bin of the histogram in figure 8.

However, one has to be very careful and remember how matplotlib.pyplot works. When different sets of data are shown in one diagram, the ones that are plotted later in the python code are printed on top of the already existing data points. This means that regions where the data overlap seem to only contain the points that came last, in our case the oldest stars. Zooming into such a transition region makes this clear. But the presence of differently coloured bands suggests that only an insignificant amount of stars with some age are above a certain stellar mass limit.

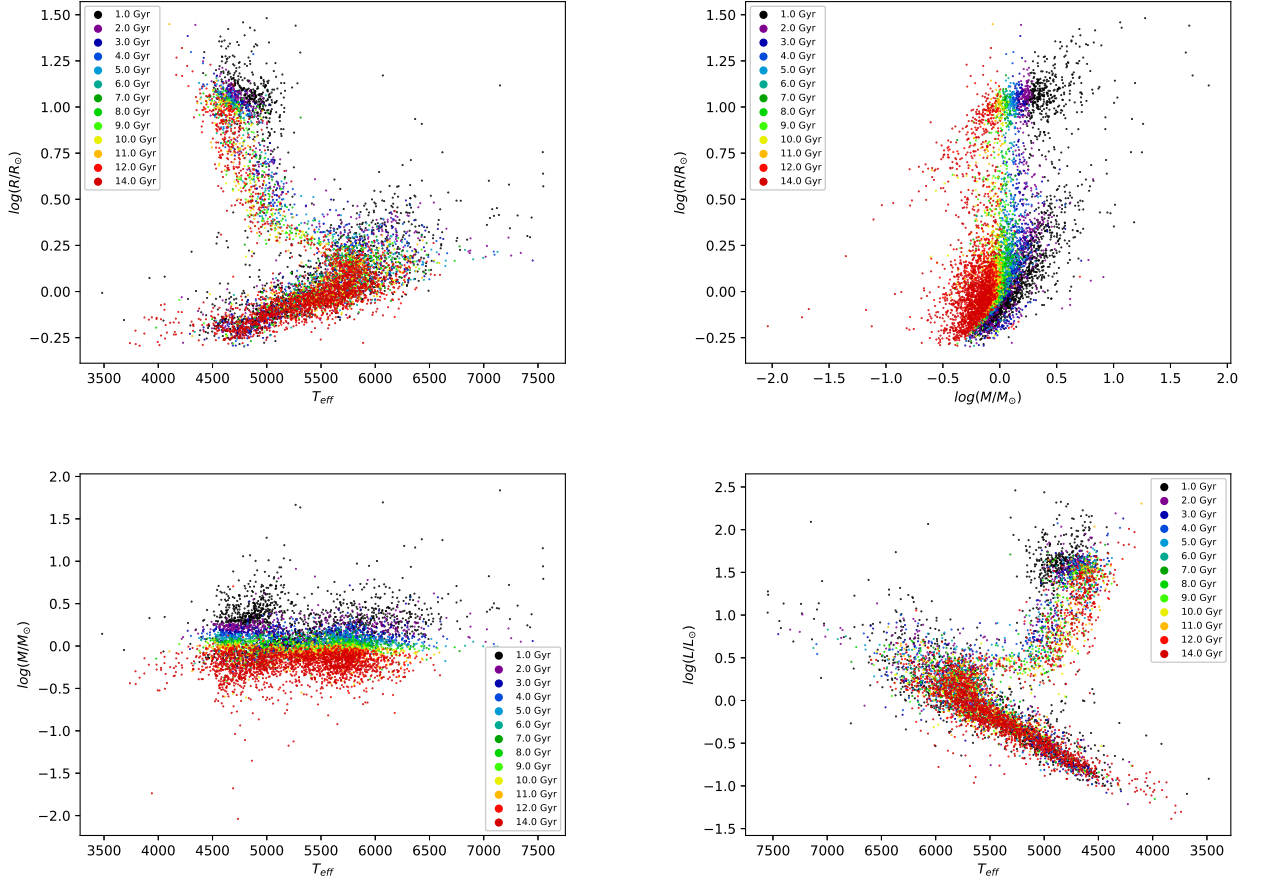


Figure 10: It is not yet exactly clear why there seem to be distinguishable areas of different ages in these 2D projections, which is of course also the case in the full three dimensional diagram.

### 4.3 Validity test

The age estimate is not good at both ends of the scale, but probably better in between. To test the performance, the algorithm should be applied to some mock data and then the results should be compared with the actual ages of the simulation. As a consequence, it is not yet clear if this "layering by age" is a hidden feature in our diagram, which is not that prominently visible in the HRD, if at all. Such a first test was done by randomly selecting 500 points out of the used isochrones with ages between 1 Gyr and 14 Gyr in steps of 1 Gyr. The expectation of the outcome is that all ages are estimated correctly. The 2D histogram in figure 11 shows the result of this first test, a diagonal distribution as one would expect. The only discrepancy is that all theoretical stars with an age of 13 Gyr are estimated to be 12 Gyr, similar to the missing bin in figure 8. It has not become clear where the source of this error is. However, since all other ages are estimated correctly we can argue that the estimate is at least not too bad. In a second step, we select again 500 random points and add some noise to make the problem more realistic. This noise is realised by adding or subtracting a small fraction of the individual quantity such that  $X_{\text{noised}} = X + aX$ , where  $X$  is  $T_{\text{eff}}$ ,  $R$ ,  $Fe/H$ , and  $M$  of each star, and  $-0.05 \leq a \leq 0.05$  is a random number representing the noise, where  $a$  is generally different for the individual quantities of one theoretical object. From appendices E, F we see that there are no dramatic differences between two consecutive sets of isochrones, meaning that some scatter around the diagonal in figure 11 is expected as shown in figure 12.

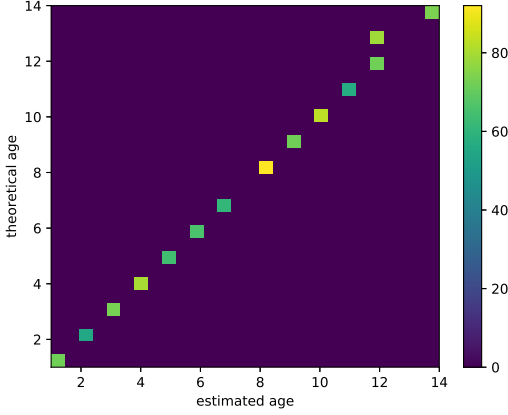


Figure 11: Besides the mentioned problem with ages of 13 Gyr the first test gives correct results, as can be expected. Some bins are much more populated than others, which is just an effect of random selection.

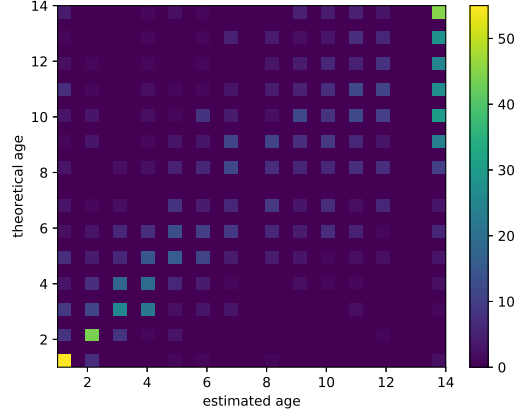


Figure 12: Like in figure 8 we see the overpopulated bins at both ends. There is indeed scatter around the diagonal which seems to increase with increasing age.

Another much simpler test would be to compare the theoretical isochrones of all  $Z$  and a fixed age together with all observed stars and see how well they match, keeping in mind that different isochrones could cross the same point in a diagram. For better visibility we only show the isochrones with  $Z$  between  $-0.5 \text{ Fe}/\text{H}$  and  $0.5 \text{ Fe}/\text{H}$ , which is the range that contains most of the stars in the data shown in figure 1. Furthermore, the isochrones are restricted to ranges in  $T_{\text{eff}}$ ,  $M$ , and  $R$  that cover the data. In this simpler test the stars are plotted by age together with the corresponding isochrones. The results can be found in appendix E. We see in these figures that there are many stars that are not covered by the shown isochrones, especially for 1 Gyr and 14 Gyr. It could be possible that isochrones with higher or lower  $Z$  could match better, but since there are only few stars with abundances different from the ones shown, this possibility is rather small. Consider for example the 14 Gyr diagram in figure 14. There are many stars on the MS above the region where the isochrones leave the MS. It is true that these stars could indeed be described by isochrones with this age and even lower metallicity. However, it might be more likely that stars in this region with  $T_{\text{eff}} \gtrsim 5800 \text{ K}$  and  $\log(L/L_{\odot}) \approx 0 - 1$  have an age somewhat below. This could be caused by comparably small uncertainties on observation, which have a non-negligible influence on the MS lifetime of a light intermediate mass star. A  $0.25 M_{\odot}$  star maintains core H-fusion for a trillion of years (Adams et al. 2005) which is orders of magnitude longer than a  $1M_{\odot}$  star, so small uncertainties in the low and intermediate mass range can change the estimated age a lot. To see if all stars in the data are covered by the theoretical values, we show the observed stars together with the isochrones of all  $Z$  in appendix F. From the figures including the masses one can see that the isochrones do not span the entire mass range covered by observation. One thing we can learn from this is why there are so many stars with an apparent age of 1 Gyr. A star with  $8M_{\odot}$  stays on the MS for only around 30 Myr (Karakas 2017), more massive stars even less. It therefore makes sense that the most massive stars that are not close to the isochrones in figures 19, 21 are sampled in the 1 Gyr bin because they are younger. This could be avoided by a higher age resolution in the calculation, but this would demand much more computation power.

## 5 Conclusion

We have introduced a new diagram in stellar astrophysics and compared it to the HRD. The  $T_{\text{eff}} - R$  plane is, as expected, very similar to the HRD but without reverse temperature axis. With stellar mass and metallicity we include the two physical quantities that determine the evolution of a star almost entirely. Although the observational data do not cover a very wide range of the different quantities, we can identify the regions that correspond to the MS and the RG in the HRD in the new diagram. It can be seen as an advantage that the radius is taken as an axis instead of the luminosity to show that stars have become RG are indeed colder and larger in size, but still with similar mass. Furthermore, because older stars tend to be metal poor and less massive than younger ones, it seems that stars with lower metallicity are more confined than in the HRD but still with some scatter and outliers.

The age estimate is not accurate enough, which is due to the design of our algorithm as well as limited theoretical data for metallicities. Therefore, it was not really possible to account for uncertainties on this quantity. If we chose a finer grid for the time steps together with a lower starting age, somewhere on the Myr scale, the algorithm would probably be able to assign some stars that are now in the 1 Gyr bin to younger ages. Looking at the mass histogram in figure 1 this would make sense, because many of the stars in the 1 Gyr bin are more massive than the Sun, with lifetimes much shorter than 1 Gyr. The ages between the ends of the scale are probably more accurate. Even if there is some deviation of  $\sim 1$  Gyr, our diagram probably has an additional feature that is not easily reproducible in the HRD. Stars with a certain age seem to only appear on a "surface" of this age, with some scatter around it. This is supported by the location of different theoretical isochrones that show a similar behaviour. As already mentioned, it would require further tests, more observational data, and additional isochrones with wider choice for metallicity to verify this.

# List of Figures

1	Several histograms that show observational data of physical quantities that are relevant for this thesis . . . . .	9
2	First published diagram by Russell, reknown as HRD . . . . .	12
3	A HRD in the popular form . . . . .	13
4	Comparison different 2D projection if $M$ or $g$ are chosen as axis . . . . .	15
5	2D projections of our new diagram compared to the HRD . . . . .	16
6	FoF algorithm applied to the data set to identify MS and GB . . . . .	17
7	Theoretical extension combined with observation . . . . .	18
8	Histogram of estimated ages . . . . .	21
9	Histogram of uncertainties on $T_{\text{eff}}$ from <i>GES</i> . . . . .	21
10	2D projections with ages as colour indication . . . . .	22
11	Age validity test without noise . . . . .	23
12	Age validity test with noise . . . . .	23
13	Close-up of figure 7 (top left) for illustrating late mass evolution . . . . .	29
14	Observed stars by estimated age combined with corresponding $T - L$ projection	30
15	Observed stars by estimated age combined with corresponding $T - M$ projection . . . . .	31
16	Observed stars by estimated age combined with corresponding $T - R$ projection	32
17	Observed stars by estimated age combined with corresponding $M - R$ projection . . . . .	33
18	All observed stars combined with the theoretical isochrones used for the age estimation in $T - L$ projection . . . . .	34
19	All observed stars combined with the theoretical isochrones used for the age estimation in $T - M$ projection . . . . .	35
20	All observed stars combined with the theoretical isochrones used for the age estimation in $T - R$ projection . . . . .	36
21	All observed stars combined with the theoretical isochrones used for the age estimation in $M - R$ projection . . . . .	37

## List of Tables

1	Data statistics . . . . .	8
2	Estimated ages . . . . .	21

## A Jeans Mass

For simplicity we assume a spherical distribution of the interstellar gas cloud with radius  $R$ , mass  $M$ , and uniform density  $\rho$ . The gravitational potential then is

$$dU = -\frac{GM(r)}{r}dM. \quad (28)$$

The mass of this sphere is just

$$M(r) = \frac{4\pi}{3}\rho r^3. \quad (29)$$

Taking the radial derivative we get the inverse of (1).

Integrating (28):

$$\begin{aligned} E_g = U &= - \int_0^R dM \frac{4\pi G\rho r^3}{r} = - \int dr \frac{dM}{dr} \frac{4\pi G\rho r^3}{r} \\ &= - \int \frac{dr}{r} \left( \frac{4\pi G\rho r^3}{r} \right) (4\pi\rho r^2) \\ &= - \int dr (4\pi\rho)^2 Gr^4 \\ &= - \frac{3GM^2}{5R}, \end{aligned} \quad (30)$$

where we multiplied  $3R/3R$  and used  $M = 4\pi\rho r^3/3$  in the last step. Assuming an ideal monoatomic gas, e.g. fully ionized hydrogen, with a uniform temperature  $T$ , the thermal energy is approximated to be

$$E_{th} = \frac{f}{2}Nk_B T = \frac{3}{2} \frac{k_B T}{m_H} \left( \frac{4\pi}{3}\rho R^3 \right) = \frac{3}{2} \frac{k_B T M}{m_H}, \quad (31)$$

where  $N$  is the total number of hydrogen atoms in the cloud, and  $m_H$  the mass of one H-nucleon. The gas cloud collapses when  $|E_g| > E_{th}$ :

$$|E_g| = E_{th} \frac{3}{5} \frac{GM^2}{R} = \frac{3}{2} \frac{k_B T M}{m_H} \quad (32)$$

Solving this for the *Jeans length*  $\lambda_J := R$  gives

$$\lambda_J = \left( \frac{5k_B T}{2m_H} \left( \frac{4\pi}{3}G\rho \right)^{-1} \right)^{1/2}, \quad (33)$$

from which the *Jeans mass*  $M_J$  follows:

$$M_J = \frac{4\pi}{3} \lambda_J \rho = \left( \frac{3}{4\pi\rho} \right)^{1/2} \left( \frac{5k_B T}{2Gm_H} \right)^{3/2}. \quad (34)$$

## B Virial Theorem

The virial theorem states that a decrease in potential energy, for example a stellar core that contracts, thermal energy has to increase. The derivation closely follows Binney & Tremaine (2008), and Teyssier (2018).

We start with the collisionless Boltzmann equation

$$\frac{\partial f}{\partial t} + \mathbf{v} \frac{\partial f}{\partial \mathbf{x}} - \frac{\partial \Phi}{\partial \mathbf{x}} \cdot \frac{\partial f}{\partial \mathbf{v}}, \quad (35)$$

where  $f$  is the distribution function and  $\Phi$  the gravitational potential. Defining a probability per unit volume  $\nu = \int d\mathbf{v} f(\mathbf{x}, \mathbf{v})$ , integrating (35) over  $\mathbf{v}$ , and make some arrangements, we are left with

$$\frac{\partial (\nu \bar{v}_j)}{\partial t} + \frac{\partial (\nu \bar{v}_i \bar{v}_j)}{\partial i} + \nu \frac{\partial \Phi}{\partial x_j} = 0 \quad (36)$$

This is multiplied by  $x_k$ , integrated over  $\mathbf{x}$ , and after some calculus we obtain

$$\frac{1}{2} \frac{d}{dt} \int d\mathbf{x} \rho (x_k \bar{v}_j + x_j \bar{v}_k) = 2T_{jk} + \Pi_{jk} + W_{jk}, \quad (37)$$

with  $T_{jk} \equiv \frac{1}{2} \int d\mathbf{x} \rho \bar{v}_j \bar{v}_k$ ,  $\Pi_{jk} \equiv \int d\mathbf{x} \rho \sigma_{jk}^2$ ,  $\rho(\mathbf{x})$  the matter density, and  $\rho \sigma_{jk}^2 = v_i \bar{v}_j \cdot \bar{v}_i \bar{v}_j$ , where we assume that  $\rho$  vanishes at large distances.  $2T_{jk} + \Pi_{jk}$  is the kinetic energy tensor,  $W_{jk}$  the potential energy tensor.

Now we rewrite the left hand side of (37) as a time dependent tensor of the form

$$\mathbf{I}_{ij} \equiv \int d\mathbf{x} \rho x_i x_j, \quad (38)$$

which is sometimes called the *moment of inertia tensor*. Considering the scalar virial theorem by taking the trace of (38), and writing  $d\mathbf{x}$  as a time dependent volume element  $dV$  this can be arranged to

$$\mathbf{I} = \int_{V(t)} dV \rho |\mathbf{x}|^2 \quad (39)$$

Taking the total time derivative this becomes

$$\dot{\mathbf{I}} = \int_{V(t)} dV 2\rho \mathbf{x} \frac{D\mathbf{x}}{Dt} = 2 \int_{V(t)} dV \rho \mathbf{x} \cdot \mathbf{v}, \quad (40)$$

where we used  $|\mathbf{x}|^2 = x^2 + y^2 + z^2$ ,  $\frac{D|\mathbf{x}|^2}{Dt} = \frac{\partial |\mathbf{x}|^2}{\partial t} + 2\mathbf{x} \cdot \mathbf{v}$ , and  $|\mathbf{x}|^2$  constant in time. If (40) is negative the system is contracting, which describes our case. The second time derivative then tells us if the contraction stops at some point (when positive) or not (when negative). Taking the time derivative and manipulating it further, this gives

$$\frac{1}{2} \ddot{\mathbf{I}} = \int_{V(t)} dV \rho v^2 + \int_{V(t)} dV \rho \mathbf{x} \cdot \mathbf{g} - \int_{V(t)} dV \mathbf{x} \cdot \nabla P, \quad (41)$$

where the first term is twice the kinetic energy, the second term is the *virial* (or force) term, and the third one is  $T - S$ , where  $T \equiv 3 \int_{V(t)} dV P$  is the term for thermal energy, and  $S \equiv \int_{S(t)} dS P \mathbf{x} \cdot \mathbf{n}$  the surface term. If there is no external pressure, as it is in general the case for stars and also assumed here<sup>16</sup>,  $S = 0$ . Further, considering a static case, we see that there are only the terms for thermal and potential energy left. Assuming energy

---

<sup>16</sup>This is not really correct, since the layers surrounding the core exert some pressure.

conservation<sup>17</sup>, if the star loses potential energy it has to become hotter, which is what we wanted to show

## C Luminosity increase

As H is converted into He, the H-abundance X decreases with time (Christensen-Dalsgaard 2008). The mean molecular weight  $\mu$  defined as

$$\mu^{-1} = \sum_i \frac{X_i(1+Z_i)}{\mu_i}, \quad (42)$$

where  $X_i$  is the fully ionised element  $i$ , and  $Z_i$  the atomic number of the respective element. Approximating this with the conditions  $Z \ll X, Y$  and  $X + Y + Z = 1$ , where  $X, Y$ , and  $Z$  are the abundances of H, He and all the metals, we get

$$\mu^{-1} \simeq \sum_j X_j + \frac{3}{4}Y + \frac{1}{2}Z, \quad (43)$$

or

$$\mu \simeq \frac{4}{3 + 5X - Z}, \quad (44)$$

which increases with decreasing hydrogen abundance. The pressure

$$P \propto \frac{\rho T}{\mu} \quad (45)$$

has to act against gravitation to keep the object in hydrostatic equilibrium. To maintain this,  $\rho T$  has to increase balancing out the higher mean molecular weight. As the star converts H into He it gets denser and hotter. As a consequence the luminosity increases.

## D M-T diagram

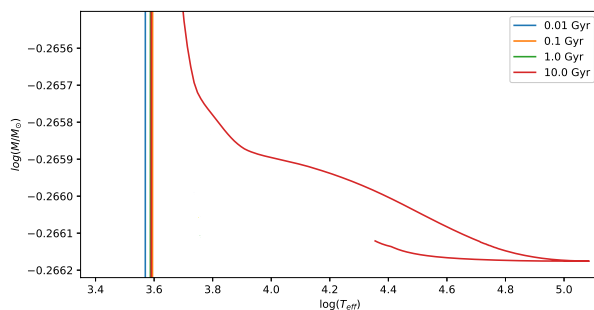


Figure 13: A closer look at the apparently horizontal lines in figure 7 shows that the WD cools down after reaching a very high temperature. This example shows the 10 Gyr isochrone.

---

<sup>17</sup>Energy conservation is not really applicable here, because a part of the energy is lost due to radiation.

## E Simple age validity test

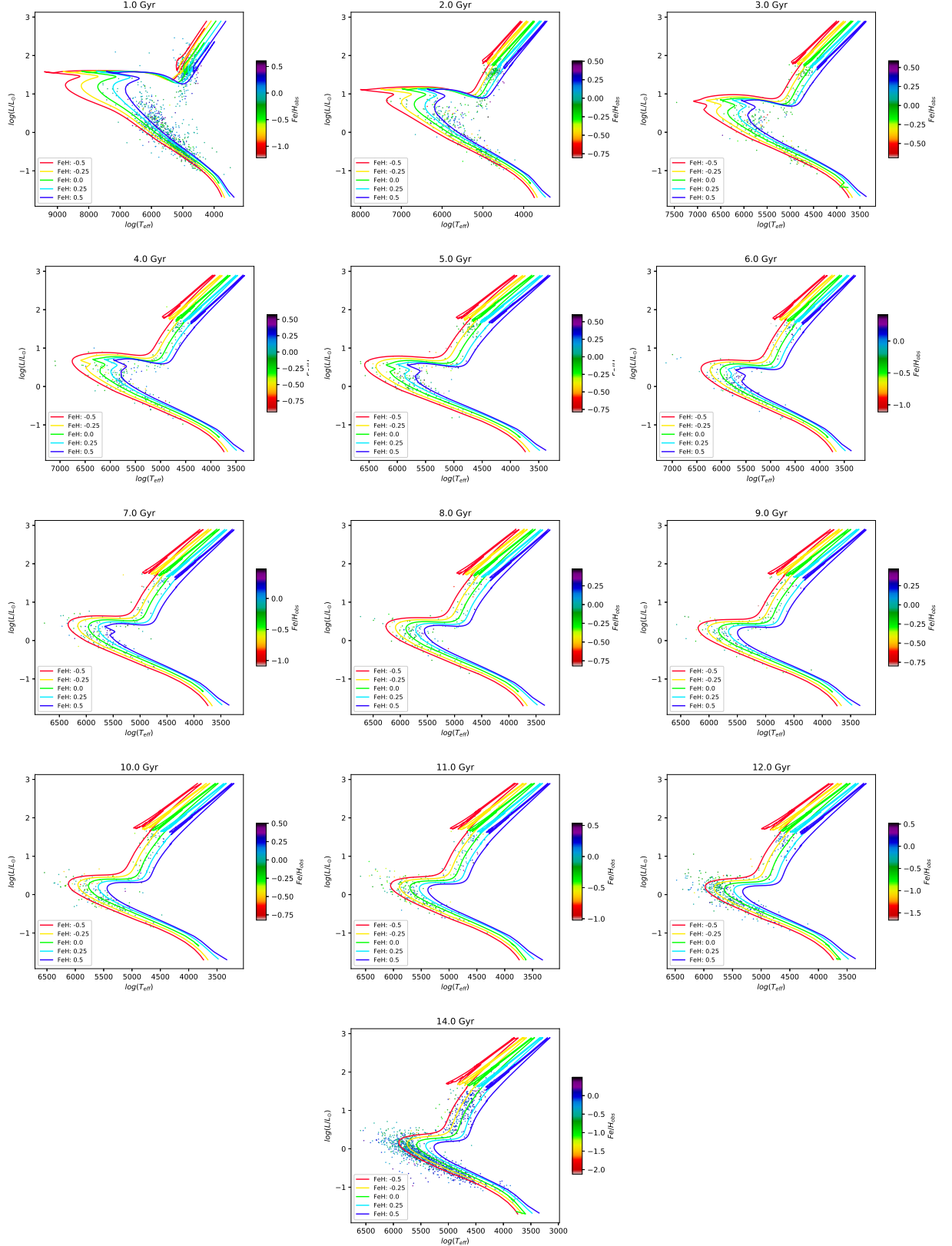


Figure 14: Observed stars by estimated age combined with corresponding  $T - L$  projection.

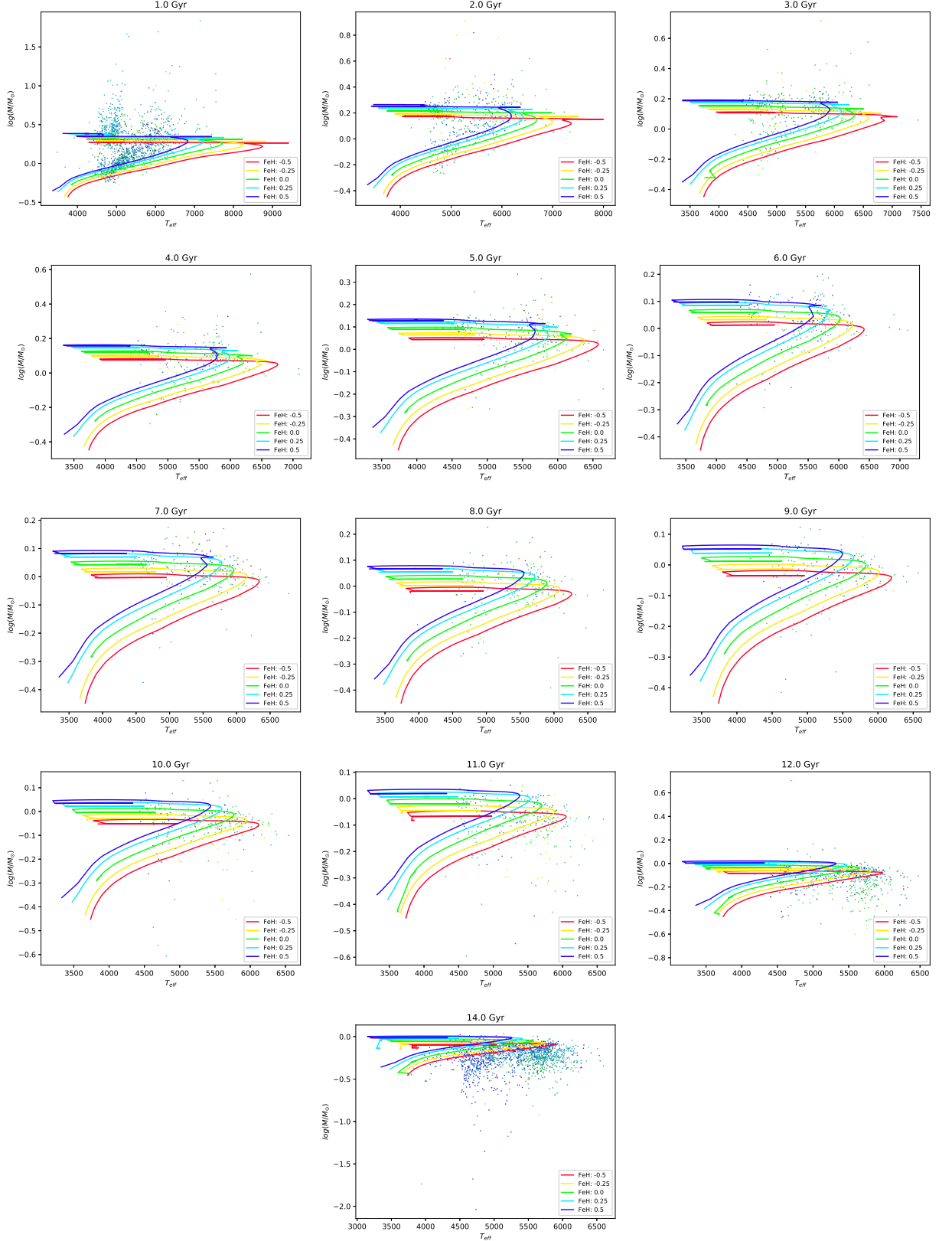


Figure 15: Observed stars by estimated age combined with corresponding  $T - M$  projection. The individual stars are coloured by metallicity as indicated by the respective colour bar in figure 14.

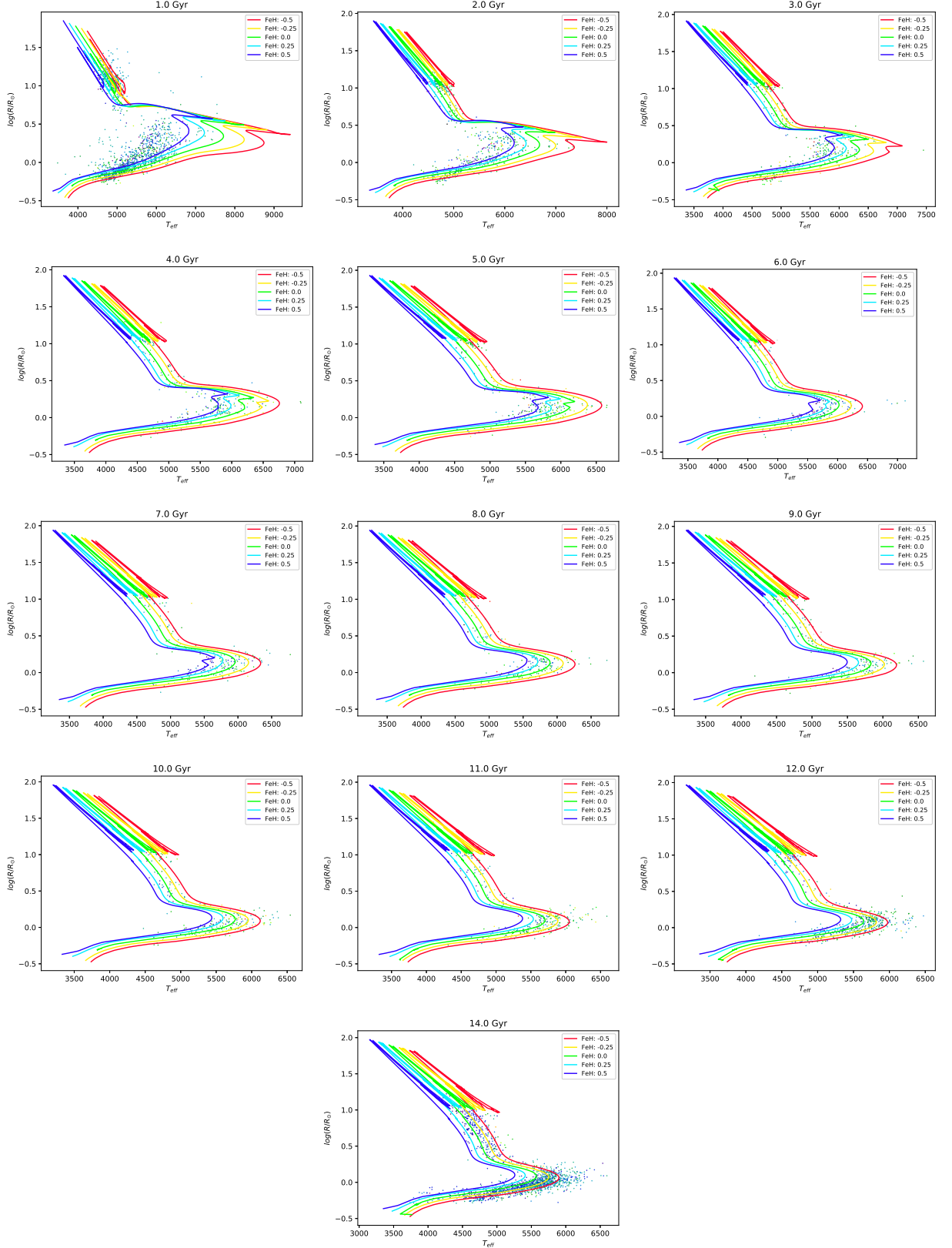


Figure 16: Observed stars by estimated age combined with corresponding  $T - R$  projection. The individual stars are coloured by metallicity as indicated by the respective colour bar in figure 14.

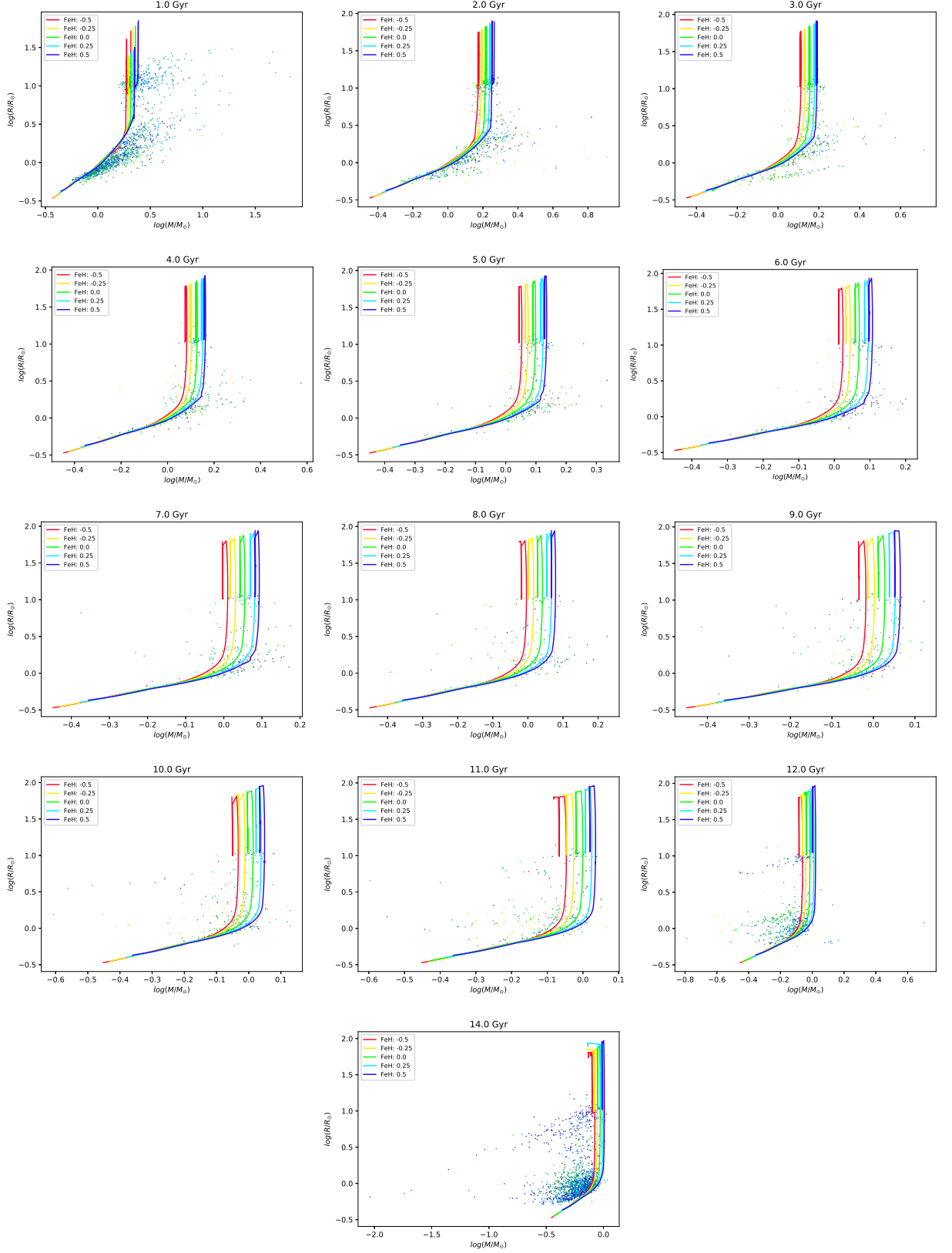


Figure 17: Observed stars by estimated age combined with corresponding  $M - R$  projection. The individual stars are coloured by metallicity as indicated by the respective colour bar in figure 14.

## F Observations and Isochrones

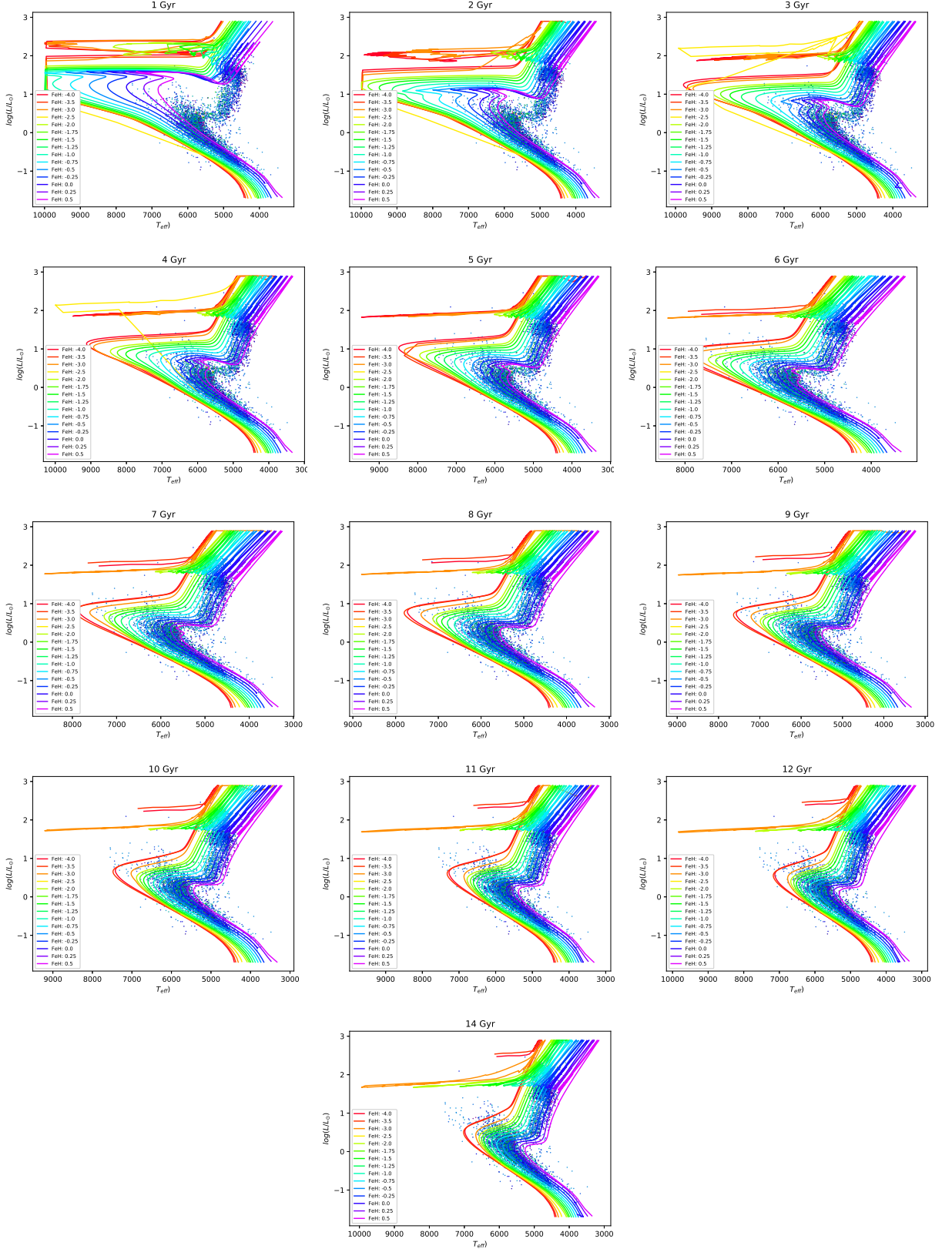


Figure 18: All observed stars combined with the theoretical isochrones used for the age estimation in  $T - L$  projection. The individual stars are coloured by metallicity as indicated by the colour bar given in figure 4.

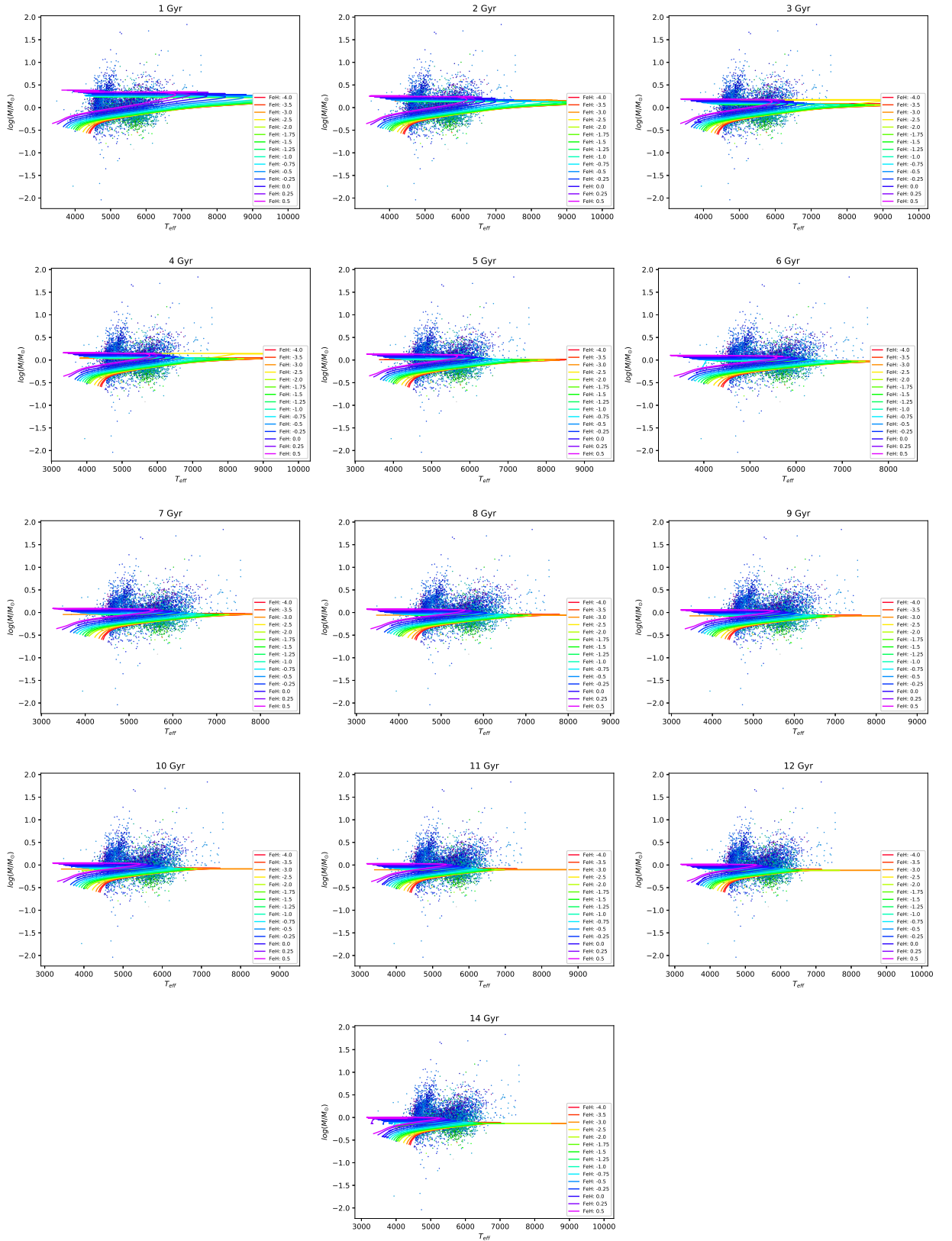


Figure 19: All observed stars combined with the theoretical isochrones used for the age estimation in  $T - M$  projection. The individual stars are coloured by metallicity as indicated by the colour bar given in figure 4.

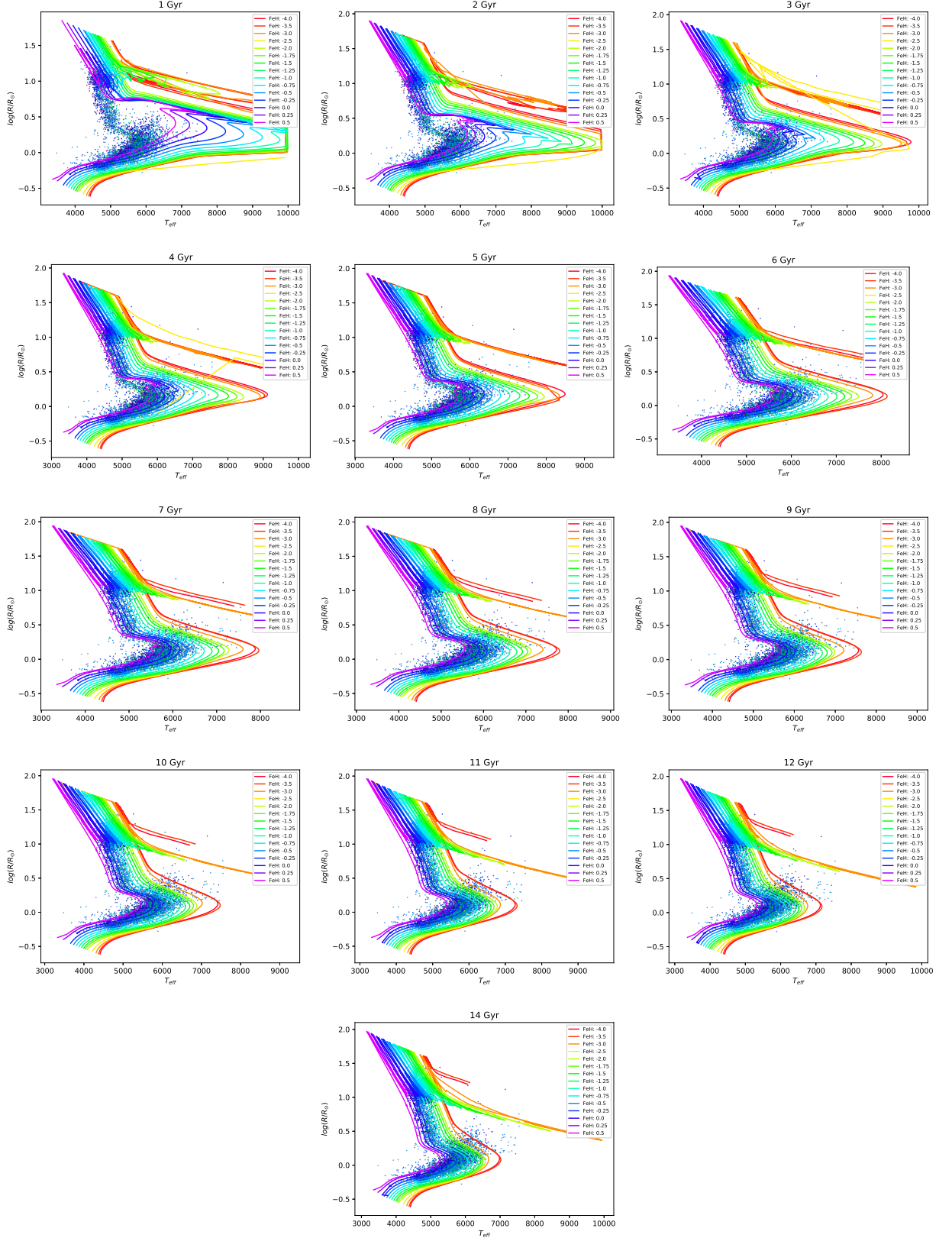


Figure 20: All observed stars combined with the theoretical isochrones used for the age estimation in  $T-R$  projection. The individual stars are coloured by metallicity as indicated by the colour bar given in figure 4.

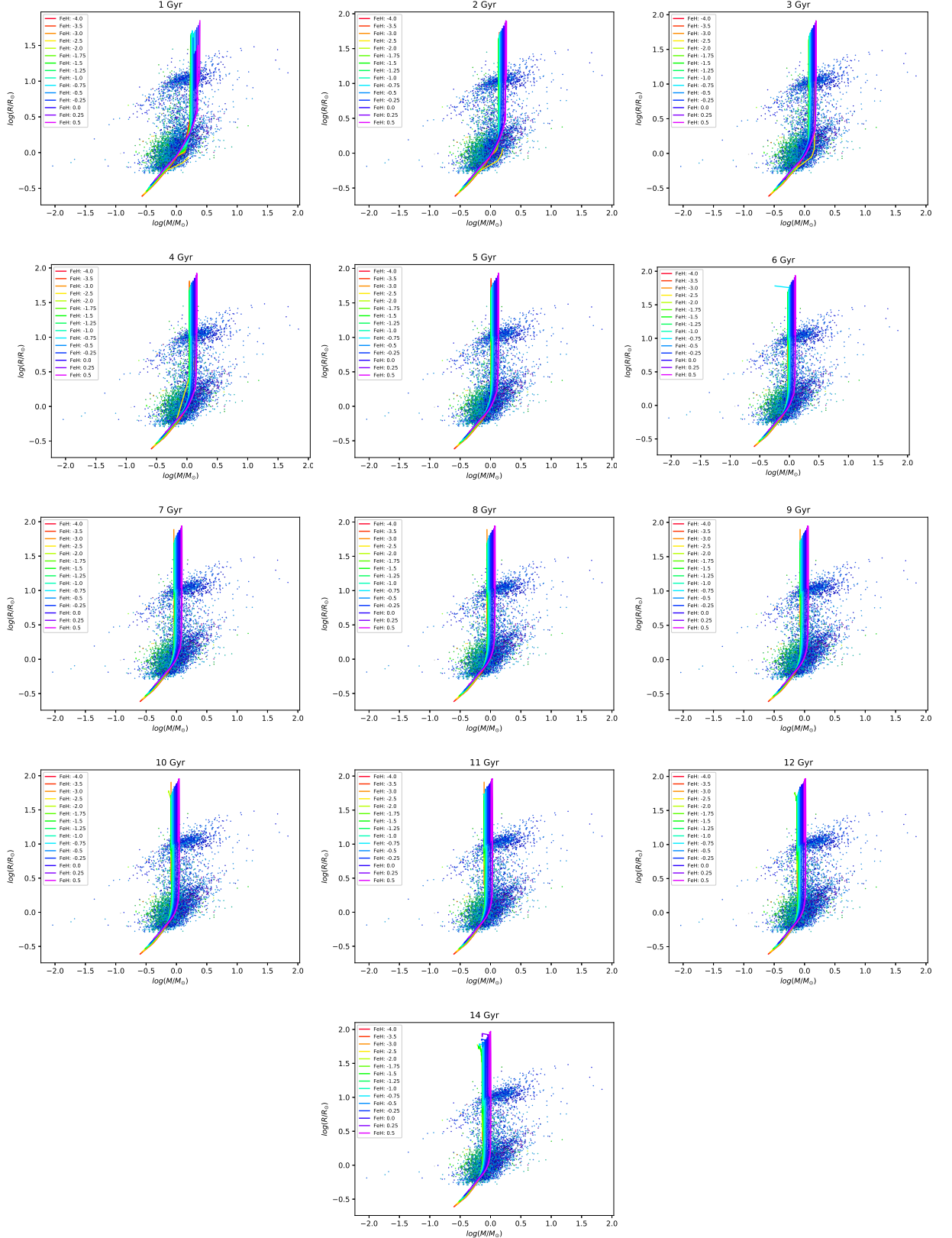


Figure 21: All observed stars combined with the theoretical isochrones used for the age estimation in  $M - R$  projection. The individual stars are coloured by metallicity as indicated by the colour bar given in figure 4.

## References

- Adams F. C., Bodenheimer P., Laughlin G., 2005, Astronomische Nachrichten, 326, 913
- Aguirre V. S., 2017, Asteroseismology and Exoplanets: Listening to the Stars and Searching for New Worlds, p. 3?25
- Bethe H. A., Brown G., 1985, Scientific American, 252, 60
- Binney J., Tremaine S., 2008, Galactic Dynamics: Second Edition. Princeton University Press
- Carroll B. W., Ostlie D. A., 2017, An Introduction to Modern Astrophysics, 2 edn. Cambridge University Press, doi:10.1017/9781108380980
- Chandrasekhar S., 1939, An introduction to the study of stellar structure. University of Chicago Press
- Choi J., Dotter A., Conroy C., Cantiello M., Paxton B., Johnson B. D., 2016, ApJ, 823, 102
- Choi J., Conroy C., Byler N., 2017, ApJ, 838, 159
- Christensen-Dalsgaard J., 2008, Lecture notes on Stellar Structure and Evolution, [https://users-phys.au.dk/~jcd/evolnotes/LN\\_stellar\\_structure.pdf](https://users-phys.au.dk/~jcd/evolnotes/LN_stellar_structure.pdf)
- Dotter A., 2016, ApJS, 222, 8
- El Eid M. F., 2018, Eur. Phys. J. Plus, 133, 372
- Gaia Collaboration et al., 2016, A&A, 595, A1
- Gaia Collaboration et al., 2018, A&A, 616, A1
- Guidry M., 2019, Stars and Stellar Processes. Cambridge University Press, doi:10.1017/9781108181914
- Hertzsprung E., 1908, Astronomische Nachrichten, 179, 373
- Hurley J. R., Pols O. R., Tout C. A., 2000, Monthly Notices of the Royal Astronomical Society, 315, 543
- Iben I., 1985, Q. Jl. R. astr. Soc., 26, 1
- Iben I., 2012, Stellar Evolution Physics. Vol. 1, Cambridge University Press, doi:10.1017/CBO9781139061223
- Jeans J. H., Darwin G. H., 1902, Philosophical Transactions of the Royal Society of London. Series A, Containing Papers of a Mathematical or Physical Character, 199, 1
- Karakas A. I., 2017, Low- and Intermediate-Mass Stars. Springer International Publishing, Cham, pp 1–21, doi:10.1007/978-3-319-20794-0\_117-1
- Kippenhahn R., Weigert A., Weiss A., 2012, Stellar Structure and Evolution, second edn. Springer, doi:10.1007/978-3-642-30304-3

- Lamers H. J., Levesque E. M., 2017, Understanding Stellar Evolution. 2514-3433, IOP Publishing, doi:10.1088/978-0-7503-1278-3, <http://dx.doi.org/10.1088/978-0-7503-1278-3>
- Larson R. B., 2003, Reports on Progress in Physics, 66, 1651
- Laughlin G., Bodenheimer P., Adams F. C., 1997, ApJ, 482, 420
- Ledoux P., 1947, ApJ, 105, 305
- MacDonald J., 2015, Structure and Evolution of Single Stars. Morgan & Claypool Publishers, doi:10.1088/978-1-6817-4105-5
- Maeder A., 2009, Physics, Formation and Evolution of Rotating Stars. Springer, doi:10.1007/978-3-540-76949-1
- Meynet G., Mermilliod J. C., Maeder A., 1993, A& AS, 98, 477
- Mo H., van den Bosch F., White S., 2010, Galaxy Formation and Evolution. Cambridge University Press, doi:10.1017/CBO9780511807244
- Nomoto K., Kobayashi C., Tominaga N., 2013, Annual Review of Astronomy and Astrophysics, 51, 457
- Paxton B., Bildsten L., Dotter A., Herwig F., Lesaffre P., Timmes F., 2011, ApJS, 192, 3
- Paxton B., et al., 2013, ApJS, 208, 4
- Paxton B., et al., 2015, ApJS, 220, 15
- Phillips A., 1994, The physics of stars. The Manchester physics series, J. Wiley, Chichester
- Pols O. R., Schröder K.-P., Hurley J. R., Tout C. A., Eggleton P. P., 1998, Monthly Notices of the Royal Astronomical Society, 298, 525
- Rose W. K., 1998, Advanced Stellar Astrophysics. Cambridge University Press, doi:10.1017/CBO9781139171205
- Rosenberg H., 1910, Astronomische Nachrichten, 186, 71
- Russell H. N., 1914, Popular Astronomy, 22, 275
- Russell H. N., Dugan R. S., Stewart J. Q., 1927, Astronomy (Boston, Ginn & Co.)
- Schwarzschild K., 1906, Nachrichten von der Gesellschaft der Wissenschaften zu Göttingen, Mathematisch-Physikalische Klasse, 1906, 41
- Soderblom D. R., 2010, Annu. Rev. Astron. Astrophys., 48, 581
- Stahler S. W., 1983, ApJ, 274, 822
- Teyssier R., 2018, Lecture notes on Theoretical Astrophysics, <https://www.ics.uzh.ch/~teyssier/teaching.html>
- Vogt H., 1926, Astronomische Nachrichten, 226, 301
- Yungelson, L. R. van den Heuvel, E. P. J. Vink, Jorick S. Portegies Zwart, S. F. de Koter, A. 2008, A&A, 477, 223